Engineering Science and Technology, an International Journal 80 (2026) 102412

Contents lists available at ScienceDirect

Engineering Science and Technology, an International Journal

journal homepage: www.elsevier.com/locate/jestch

Full Length Article

LMI-based adaptive-robust traffic signal control with disturbance feedforward for mixed traffic with CAVs

Arshia Abdi [a], Bijan Moaveni [b], Tamás Tettamanti [c,d],*

[a] Department of Systems and Control Engineering, Faculty of Electrical Engineering, K. N. Toosi University of Technology, Seyed-Khandan, Shariati Ave., Tehran, 1631714191, Iran
[b] Department of Systems and Control Engineering, Center of Excellence for Modeling and Control of Complex Systems, K. N. Toosi University of Technology, Seyed-Khandan, Shariati Ave., Tehran, 1631714191, Iran
[c] Department of Control for Transportation and Vehicle Systems, Faculty of Transportation Engineering and Vehicle Engineering, Budapest University of Technology and Economics, Műegyetem rkp. 3, Budapest, H-1111, Hungary
[d] Systems and Control Laboratory, HUN-REN Institute for Computer Science and Control, Kende u. 13-17, Budapest, H-1111, Hungary

ARTICLE INFO

Keywords:
Urban traffic control
Adaptive-robust control
Linear Matrix Inequality (LMI)
Connected and Autonomous Vehicle (CAV)
Feedforward disturbance rejection
Mixed traffic flow

ABSTRACT

This study develops a two-level adaptive-robust traffic signal control architecture that combines an LMI-synthesized, intersection-level robust state-feedback regulator with a measurable inflow feedforward channel and a Connected and Autonomous Vehicle (CAV)-aware operational layer. The proposed adaptive-robust LMI-based control method considers the uncertainty as the effect of saturation flow via a small polytopic set and enforces a quadratic Lyapunov certificate via LMIs to guarantee uniform exponential queue regulation across the modeled vertices. A key innovation of this approach is the inclusion of a measurable disturbance feedforward mechanism that proactively compensates for short-horizon inflow surges, thereby reducing the reactive burden on the feedback loop. Furthermore, the control strategy features a CAV-aware adaptive operational layer that dynamically adjusts the conservatism of the robust synthesis based on real-time traffic composition, switching to a lightweight LQR fallback when necessary. The proposed method is validated using real traffic data from Tehran city, mimicked within a validated microsimulation (SUMO) environment. Comparative experiments demonstrate that the proposed control method significantly outperforms in reducing delays and emissions. Additionally, computational feasibility (milliseconds execution time) is guaranteed compared to the high latency of AI-based approaches.

1. Introduction

Urban transportation networks worldwide are grappling with increasing traffic congestion, which negatively impacts travel time reliability, air quality, and energy consumption. Effective and timely traffic signal control is paramount to mitigating these challenges. Traditional control strategies, such as fixed-time plans or simple reactive methods, often fail to adapt efficiently to the complex, stochastic, and dynamic nature of modern urban traffic flow, especially during peak hours or in the presence of unforeseen incidents [1–3]. This limitation necessitates the development of sophisticated control methodologies capable of managing network-wide performance while explicitly accounting for various sources of uncertainty and variability, such as fluctuating demand, changes in saturation flow [4], and unpredictable driver behavior.

1.1. Robust control approaches for urban traffic

A significant body of research has focused on applying control theory, particularly robust control, to guarantee system stability and performance despite uncertain inputs. Early work formulated the traffic signal design problem as a robust optimal control strategy, recognizing that future transportation demand is inherently uncertain [1]. Subsequent efforts introduced the use of Linear Matrix Inequality (LMI) techniques and state-space representations to model the uncertain network system using linear polytopic approaches, leading to the development of robust and infinite-horizon Model Predictive Control (MPC) strategies to handle model mismatches and reduce travel time [5].

The extension of robust control principles to urban road networks has seen formulations aimed at minimizing weighted link queue lengths under the influence of unknown but bounded demand and queue

* Corresponding author at: Department of Control for Transportation and Vehicle Systems, Faculty of Transportation Engineering and Vehicle Engineering, Budapest University of Technology and Economics, Műegyetem rkp. 3, Budapest, H-1111, Hungary.
E-mail address: tettamanti.tamas@kjk.bme.hu (T. Tettamanti).

https://doi.org/10.1016/j.jestch.2026.102412
Received 19 February 2026; Received in revised form 15 April 2026; Accepted 16 May 2026
Available online 7 June 2026

uncertainties [6]. These approaches often rely on centralized minimax optimization, which minimizes the objective function under the worst-case uncertainty realization. The robust control strategy for oversaturated intersections has also been addressed by modeling the system as a discrete-time switched system and determining green times via a set of linear state feedback controllers, which are designed using LMI techniques to estimate and minimize the boundary of waiting queue length [7]. While recent data-driven methodologies, such as Spatio-Temporal Graph Neural Networks (ST-GNN) [8] and deep learning-based wavelet transforms [9], have demonstrated superior accuracy in bottleneck prediction and signal optimization, integrating these predictive capabilities into a control loop that retains formal stability guarantees remains a primary motivation for robust control frameworks.

Furthermore, research on network-wide control has also investigated the use of robust perimeter control. By incorporating time delays and unknown bounded external disturbances within a Macroscopic Fundamental Diagram (MFD)-based model structure, robust control architectures have been designed for one or multiple aggregated urban traffic regions [10,11]. Complementary to perimeter control, recent reviews highlight the potential of emerging internal boundary control and lane reversal strategies to manage bidirectional capacity and tidal flows in future traffic networks [12]. These methods provide a fixed controller structure with constant gains to compensate for uncertainties, focusing on the worst-case scenario concept. The application of LMI methods has also been essential in analyzing and synthesizing robust controllers in related fields, such as stabilizing bilinear systems with state-based switching which can approximate certain nonlinear traffic dynamics [13]. More recently, LMI has been used to obtain control and observation gains for observer-based double closed-loop control strategies in mixed vehicle groups, ensuring convergence and stability [14].

A key finding in the area of robust control, specifically in subway networks which share dynamic characteristics with road networks, demonstrates the efficacy of robust state feedback controllers in compensating for delays caused by disturbances in intersecting lines, using LMI for controller design [15]. This reinforces the potential of robust state feedback structures for infrastructure-based traffic control.

1.2. Hierarchical and two-level control architectures

Managing the inherent complexity and large scale of urban traffic networks necessitates control architectures capable of decoupling the problem into manageable, interconnected layers. Hierarchical frameworks are a prominent approach that addresses computational intractability and complexity by partitioning the network control problem into different levels of abstraction and time scales. These architectures typically involve an upper-level layer and a lower-level layer. The upper-level layer often operates on a macroscopic time scale, utilizing concepts such as the MFD for large-area demand-balance and perimeter control [16]. This layer focuses on strategic objectives like optimizing region-wide flow and managing network loading (e.g., [10,11]). Conversely, the lower-level layer executes control at a shorter time scale, focusing on tactical objectives such as determining optimal local signal timing, trajectory planning, or utilizing detailed flow models and distributed schemes for local intersection management [16–18].

At the network level, observer-based double-loop controllers combine a macro-level controller for region-scale flows with an inner loop that controls local actions, such as ramp metering or platoon speed [14]. These observer architectures suggest practical ways to fuse sparse measurements and to obtain robust short-horizon predictions of inflows and queue evolutions. This need for real-time local prediction aligns with advanced methods such as using Long Short-Term Memory (LSTM) networks deployed at the edge to predict the network state for efficient, decentralized resource allocation in vehicular communication systems [19]. Micro-macro integrated approaches explicitly reconcile network-wide objectives with vehicle-level actuation. Recent work on combined macro–micro strategies demonstrates how macroscopic references can be enforced through microscopic platoon maneuvers and speed commands, while maintaining scalability.

The control methods employed within these layers vary. For instance, some utilize MPC at both levels, refined for computational efficiency by techniques such as using the Link Transmission Model (LTM) to explicitly incorporate complex dynamics like upstream propagating waves (spillback) into linear optimization problems [20]. Other variations include bi-level optimization frameworks, where the upper level evaluates strategic parameters (like green light and cycle durations) to expand the control space, while the lower level handles synchronization and flow optimization based on those strategic inputs [21]. Furthermore, the concept extends to microscopic vehicle control, where a hierarchical optimization is used, such as planning a leading vehicle's trajectory (high-level) and optimizing the following vehicles via rolling optimization (low-level) to enhance eco-driving for Connected and Autonomous Vehicle (CAV) platoons [22]. The necessity of this multi-level approach is further underscored by recent work on cooperative platoon merging, which explicitly combines macroscopic network-wide traffic control with microscopic individual vehicle dynamics to achieve a scalable solution in mixed traffic flows [23].

1.3. CAVs and mixed traffic systems

The penetration of CAVs introduces a sample shift by providing rich data and vehicular actuation capabilities. Research in this domain can be categorized into two main streams: (1) Signal Control Augmentation and (2) Cooperative Vehicle-Platoon Control.

1.3.1. Signal control augmentation in mixed traffic

Control systems are being augmented by incorporating data from CAVs (e.g., position, speed) alongside traditional loop detectors. Algorithms like Multi-mode Adaptive Traffic Signals (MATS) demonstrate significant delay reduction even with low CAV penetration rates [24]. This is complemented by data-driven traffic flow models, such as hybrid ARIMA-Prophet approaches, used in edge environments to enhance forecasting accuracy and reduce latency for local decision-making [25].

Furthermore, the use of extended observers (EO) based on Extended Kalman Filters (EKF) enables accurate queue length estimation and prediction using limited CAV measurements, especially in oversaturation, facilitating their integration into existing Urban Traffic Control (UTC) systems [26]. Joint optimization of signal control and CAV speed planning is a complex problem, often tackled using bi-level robust optimization frameworks that employ Dynamic Programming (DP) and Pontryagin's Minimum Principle (PMP) to minimize total cost (delay and fuel) while explicitly dealing with stochastic driver behavior via robust optimization techniques [27]. Hierarchical cooperative eco-driving controllers have also been proposed for CAV platoons at successive signalized intersections, planning the leading vehicle's trajectory via the pseudo-spectral method and optimizing following vehicles via rolling optimization [22].

In a related direction, recent work has explored learning-based approaches for mixed traffic coordination. For instance, [28] proposes a two-stage framework for mixed vehicle platoon formation, where feasible platoon configurations are first generated and subsequently refined using multi-agent reinforcement learning. This approach highlights the potential of integrating data-driven coordination strategies with traffic control in mixed CAV–HDV environments. These developments further motivate the need for control frameworks that can systematically integrate microscopic coordination with macroscopic traffic management.

1.3.2. Platooning, robustness, and dynamics

For a complex dynamic system as urban traffic, distributed control is crucial for scalability. Studies on platooning often focus on string stability and disturbance rejection. Robust H_∞ control strategies are widely used to stabilize traffic flow against disturbances (e.g., abrupt deceleration) and parametric uncertainties inherent in Human-Driven Vehicle (HDV) dynamics, particularly in mixed platoons with a single CAV [29–31]. These solutions leverage graph theory and spectral decomposition to handle platoon dynamics with undirected topologies and heterogeneous time delays [32,33]. The application of MPC is also prominent in path tracking for individual autonomous vehicles, where optimized kinematic models are used to enhance tracking performance and stability [34]. A recent comprehensive review further systematizes trajectory planning and tracking control strategies for autonomous driving, emphasizing the integration of optimization-based methods with machine learning and deep learning techniques to improve robustness and real-time feasibility under uncertainty [35]. The survey highlights the tight coupling between high-level trajectory generation and low-level tracking controllers, underscoring the importance of stability-oriented control architectures in autonomous traffic environments. Distributed integrated sliding mode control (SMC) has also been developed using disturbance observers to estimate nonlinear uncertainties in vehicular systems, enhancing string stability and traffic density [36]. A recent hierarchical approach was proposed for oscillation mitigation in mixed platoons, using a two-layer structure: Oscillation-Optimized Feedforward Control (OOFC) for CAVs and Speed-Perception-Enhanced Control (SPEC) for HDVs, demonstrating significant reductions in speed fluctuations [37].

The clustering strength of CAVs, defined by metrics like the autocorrelation-based platooning intensity (API), has been shown to be a critical factor influencing mixed traffic capacity, with stronger clustering not always guaranteeing capacity improvement due to headway stochasticity [38].

Furthermore, detailed flow modeling using advanced machine learning methods, such as the improved Group Method of Data Handling (GMDH) compared to Artificial Neural Network (ANN), is increasingly used to accurately capture the complex nonlinear dynamics of mixed vehicular traffic flow on freeways, enhancing the fidelity of predictive tools [39].

This highlights the need to accurately model the impact of CAVs on macroscopic flow parameters. Recent studies have extended platoon-level control concepts toward corridor-level congestion mitigation in mixed traffic environments by explicitly modeling the interaction between CAV platoons and macroscopic traffic dynamics. In particular, [40] proposes a V2X-enabled cooperative platoon control framework based on a dynamic platoon-embedded cell transmission model, where moving bottlenecks are strategically regulated to mitigate aperiodic congestion and improve network-wide traffic efficiency. In a related direction, [41] develops a two-stage adaptive control framework that integrates model predictive control with front-tracking methods to address mixed-traffic congestion through coordinated speed regulation and moving bottleneck control. These approaches highlight the importance of coupling microscopic platoon behavior with macroscopic traffic flow models for effective large-scale congestion mitigation. The integration of macro–micro modeling is also gaining traction, where macroscopic network-wide models optimize speed limits and ramp metering (high-level control), and microscopic models plan individual vehicle trajectories (low-level control), offering a scalable solution for cooperative platoon merging [23]. These developments further reinforce the need for integrated macro–micro control architectures, where local vehicle-level coordination and network-level optimization are jointly considered.

1.4. Decentralized control architectures and scalable optimization

From a classical control perspective, several decentralized schemes have been developed to manage large-scale systems without requiring global optimization. One powerful approach utilizes Decentralized Control derived from LMI formulations. For instance, overlapping decentralized control schemes efficiently transform the overall Linear Quadratic (LQ) control problem into an LMI problem, allowing for a structured gain matrix that enables decentralized deployment in real-time with efficiency comparable to centralized solutions [42]. This method directly supports the goal of utilizing LMI for robust yet scalable solutions.

This shift toward decentralized decision-making is also strongly supported by advancements in Multi-Agent Deep Reinforcement Learning (MADRL), which integrates predictive models (like LSTM) to proactively optimize resource allocation and enhance network performance in edge-enabled vehicular networks, thereby offering a highly scalable and adaptive control framework [19]. In parallel, data-driven adaptive control approaches have been proposed for constrained nonlinear multi-agent systems, where locally linearized dynamic models are identified online from input–output data and the control problem is reformulated as a constrained quadratic program solved in real time [43]. Such frameworks demonstrate how model-light, stability-certified optimization schemes can be deployed in interconnected large-scale systems, which is conceptually aligned with scalable urban traffic control architectures. Furthermore, Adaptive Linear-Quadratic Regulator (LQR) strategies have been designed to manage large urban networks by building and adaptively updating a linear dynamic traffic system model. This model-based adaptive LQR achieved superior computational feasibility and lower average delays compared to centralized state-of-the-art methods, underscoring the value of computationally light, adaptive control-theoretic solutions [44]. The analysis of decentralized control for heterogeneous urban grid networks further suggests that controllers integrating both upstream and downstream congestion information are more robust and effective in achieving network stability, demonstrating the localized benefits of using neighborhood information [45].

1.5. Adaptive operation, gain scheduling and LMI-based synthesis

Traffic patterns evolve slowly across the day and exhibit regime changes between peak and off-peak periods. A pragmatic way to exploit this structure is to maintain a simple nominal model that is periodically updated and to switch between controllers that are designed for representative operating regimes. Gain scheduling and identify then control paradigms have been studied for similar problems, where a bank of precomputed gains or an online re-synthesis procedure is used to adapt the controller to the current estimated operating point [44,46].

The efficacy of such adaptive frameworks heavily relies on accurate, real-time prediction of traffic states. Modern approaches utilize deep learning models, such as LSTM and Gated Recurrent Unit (GRU) integrated with wavelet denoising, to capture the inherent nonlinearity and temporal dependencies of traffic data, thus providing the necessary foundation for reliable mode decision and re-synthesis procedures [9].

LMI-based state feedback synthesis integrates naturally into such an adaptive architecture since LMI conditions can be enforced for a small set of representative model vertices to obtain gains that are robust for a local uncertainty polytope. The LMI framework also permits imposing a quadratic Lyapunov certificate that guarantees exponential decrease of a chosen energy function across all vertices. Practical online operation, however, faces two principal computational and numerical challenges. First, frequent re-synthesis may be computationally demanding. Hence, a careful mode decision mechanism is required to trigger re-synthesis only when identification confidence and computational budget permit. Second, numerical infeasibility or ill conditioning may occur under low excitation or under strong uncertainty. Therefore, a robust, low-cost fallback such as an LQR-based gain computed from a nominal model can provide a principled safety net that maintains stable operation when the primary synthesis is unavailable.

The literature contains several contributions that combine model updates with reactive compensation and that analyze convergence and performance of such schemes [11,46]. These results support the use of periodic model adaptation combined with a local reactive controller. Our approach builds on these insights but departs from prior work in two important aspects. First, we explicitly exploit measurable inflows inside the synthesis in a feedforward architecture that integrates with the LMI-based state feedback. Second, we tie the adaptation logic to an online assessment of traffic composition, notably to the penetration of CAVs, which directly reduces uncertainty in the input mapping.

1.6. Research gaps and motivations

The extensive body of literature reviewed provides a robust foundation in both traffic signal control and vehicular dynamics, but also reveals several persistent gaps that motivate the present study.

- Decentralized Robust Synthesis With Scalable Online Feasibility: While robust control based on LMI and H_∞ methods offers strong stability guarantees for polytopic uncertainty [6,7], these formulations are often utilized in centralized settings or require heavy computational loads associated with MPC [20, 47]. This complexity creates significant scalability and implementation barriers for decentralized real-time deployment at the intersection level. A critical need exists for a decentralized framework that retains formal robustness certificates (e.g., Lyapunov stability) while remaining computationally tractable for online re-synthesis, a challenge often faced by pure LMI techniques [42]. This gap is particularly highlighted by advanced decentralized approaches, such as Spatio-Temporal Graph Neural Networks (ST-GNN) for signal optimization [8] and MADRL for resource allocation [19], which, while offering high scalability, often lack the formal robustness certificates and worst-case performance guarantees intrinsic to control-theoretic designs.
- Limited Integration of Measurable Inflow Disturbances in LMI-Based Control: Existing robust state feedback designs, including LMI-based syntheses, typically focus on compensating for internal model uncertainties or unknown but bounded external disturbances using only the feedback loop [10,15]. They often fail to fully exploit easily measurable short-horizon inflow information (such as current turning movement volumes or upstream queue spillback) as a modular feedforward term inside the control loop. Practical exploitation of these measurable inflows, which allows for proactive compensation of predictable demand surges, has received limited attention in formal LMI frameworks, leading to overly reactive control responses [45]. The need for proactive compensation is further intensified by the success of deep learning in precise traffic flow prediction [9], which provides high-quality, denoised data that should ideally be utilized as a feedforward term to reduce the control effort required by the robust feedback loop.
- Lack of Adaptive Robustness Tuning Under CAV Penetration Variability: The literature recognizes that the presence of CAVs fundamentally reduces the stochasticity of traffic flow and improves stability in mixed platoons [30,38]. However, most robust controllers, designed for the worst-case scenario using static uncertainty bounds, fail to dynamically link online controller re-synthesis decisions to empirical measures of CAV penetration. The conservatism inherent in static worst-case robust design is not mitigated as the traffic flow becomes more deterministic due to increasing CAV presence, resulting in suboptimal performance when certainty is high. A principled, adaptive mechanism is needed to use empirical CAV statistics to trigger LMI-based re-synthesis, thereby dynamically reducing the robustness margin and improving average performance, an area that remains underdeveloped [44,46]. Moreover, advancements in high-fidelity traffic flow modeling, such as the comparative analysis demonstrating the superior predictive performance of GMDH over ANN in complex vehicular flows [39], provide empirical justification for developing adaptive controllers that can leverage these improved models to dynamically adjust the uncertainty set based on the current traffic composition.
- Need for Real-Time Resilience Through a Guaranteed Fallback Strategy: The transition from theoretical robust synthesis to practical, continuously operating systems introduces computational and numerical challenges. Online re-synthesis of LMI gains, although desirable for adaptation, may encounter numerical infeasibility or high processor demand, resulting in occasional failures [44]. Therefore, a robust and lightweight fallback mechanism, such as a stable LQR gain derived from a nominal model, is essential to maintain safe and stable operation when the primary adaptive synthesis process is temporarily unavailable, ensuring real-time reliability in a decentralized setting.

1.7. Main contributions

To address the gaps identified above, this paper proposes a novel integrated control architecture that is a two-level adaptive-robust traffic signal control with LMI synthesis and disturbance feedforward in mixed traffic with CAVs for decentralized traffic signal systems operating in mixed CAV-HDV environments. The contributions of this work are listed below.

- We develop a decentralized LMI-based robust state feedback design that provides a Lyapunov-based certificate of exponential queue stability for a local uncertainty set of input mappings. The synthesis is intentionally designed to be computationally lightweight and decoupled, allowing it to be executed at the intersection level and realizing an efficient online solution. The design leverages polytopic uncertainty representations and convex semidefinite programming to produce gains that are robust across modeled vertices.
- We introduce an integrated measurable disturbance feedforward component that proactively consumes short-horizon inflow measurements and upstream queue information to compensate exogenous arrivals inside the control loop. This component is designed to operate seamlessly alongside the LMI state feedback structure, reducing transient queue growth and improving overall transient performance, thereby decreasing the reactive burden on the feedback adaptation mechanism.
- We propose a CAV penetration-aware adaptive operational layer that conditions the online re-synthesis of the robust controller on empirical indicators of traffic composition, specifically measured CAV penetration. When the estimated composition implies reduced uncertainty in the input mapping, the system attempts an online LMI re-synthesis with a dynamically reduced conservatism margin. When re-synthesis is infeasible or identification fails acceptance tests, the controller switches to a computationally light LQR fallback that guarantees stable operation.
- We provide practical identification and mode decision rules together with numerical safeguards for online LMI synthesis. These elements bridge the gap between offline theoretical synthesis and robust real-time deployment, and clarify how the decentralized, adaptive controller scales when multiple intersections operate in parallel. Crucially, these rules also define the interface by which microscopic traffic composition (CAV presence) informs the macroscopic queue regulation model, maintaining the integrity of the two-level control concept.

- We present a comprehensive validation methodology in Simulation of Urban MObility (SUMO) software [48] using real traffic data from Tehran city. The evaluation explores a range of CAV penetration levels, and benchmarking compares the proposed method against fixed-time plans, fixed-time with platooning, SUMO gap-actuated adaptive control, and a zero-shot Large Language Model (LLM) advisor-style baseline. The experimental study reports both traffic performance metrics and computation and processing times, focusing on a critical comparison of real-time feasibility between the proposed method and the AI-based baseline, to assess scalability.

The remainder of the paper is organized as follows. Section 2 formalizes the modeling assumptions and the discrete-time per-cycle state representation. Section 3 details the LMI-based synthesis, the disturbance feedforward design, the online identification tests, and the fallback strategy. Section 4 presents the simulation setup, the experimental scenarios across CAV penetration rates, and the benchmarking methodologies. Section 5 discusses results and limitations, and section six concludes with final remarks and avenues for future work.

2. Urban traffic modeling

In this section, a two-level modeling framework is introduced in which macroscopic and microscopic representations of traffic dynamics are treated as separate yet coordinated layers. Due to fundamental differences in temporal resolution, data abstraction, and modeling objectives, these two levels are not merged into a single unified mathematical formulation. Instead, they interact through a structured bidirectional information exchange mechanism. To make the interaction between the two levels explicit, the proposed framework is implemented as a closed-loop hierarchical system with bidirectional coupling. At each signal cycle, the macroscopic layer computes the green time allocation $U(n)$ based on aggregated traffic states. These control actions are then propagated to the microscopic layer, where they directly influence vehicle motion, signal compliance, and platoon evolution.

Conversely, the microscopic layer continuously generates high-resolution traffic data, including vehicle counts, discharge rates, queue lengths, and platoon characteristics. These quantities are aggregated over each cycle and fed back to the macroscopic layer to update the system state $X(n)$, estimate the time-varying matrix $B(n)$, and refine the control decisions. Therefore, the macroscopic model is not static but dynamically influenced by the evolving microscopic traffic conditions. The macroscopic layer captures aggregated traffic evolution and produces supervisory control decisions such as signal phase timing, whereas the microscopic layer describes detailed vehicle-level dynamics, including CAV-enabled platoon formation and motion control. This hierarchical coordination exploits the complementary strengths of both modeling scales while avoiding the computational complexity and scalability limitations associated with fully integrated multi-scale formulations.

2.1. Macroscopic level

At the macroscopic level, the traffic dynamics are described by defining the number of vehicles approaching an intersection along each street as the system state, denoted by $x_l(\cdot)$. Accordingly, the number of vehicles on street l at the subsequent event instant $n+1$, namely $x_l(n+1)$, is determined as shown in Eq. (1). This evolution depends on the previous accumulation $x_l(n)$, the incoming traffic demand $q_l^{in}(n)$, the departing flow $q_l^{out}(n)$, and the control variable $u_j(n)$, where index j corresponds to the independent signalized directions at the intersection.

The macroscopic traffic model follows an event-based formulation in which the discrete index n represents phase change events rather than uniform sampling instants. Each transition of the traffic signal, such as switching from green to red or vice versa, constitutes a single event. A complete signal cycle is therefore completed over two consecutive events, corresponding to the interval $[n, n+2]$. The total duration of this interval is equal to the predefined cycle time CT. Although the individual phase durations may vary across events, their cumulative length over two events remains fixed and equal to CT.

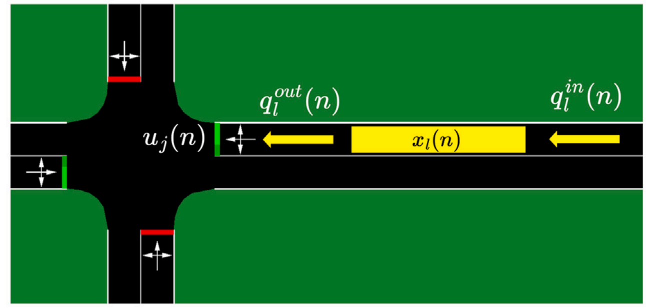

Fig. 1. Schematic representation of the key variables used to characterize traffic dynamics at a signalized intersection.

To avoid ambiguity between event-based indexing and cycle-based control interpretation, the temporal structure of the model is clarified as follows. The discrete index n is associated with signal switching events, whereas the control input $U(n)$ is defined at the cycle level and applied over the interval $[n, n+2]$. Specifically, each control update occurs once per cycle, i.e., after two consecutive events.During the interval $[n, n+2]$, the control input $U(n)$ remains constant and determines the green time allocation for the entire cycle. The first event at index n corresponds to the beginning of a phase (e.g., green onset for a given direction), while the second event at $n+1$ corresponds to the switching to the competing phase. The cycle is completed at event $n+2$, at which point new state measurements are collected and a new control input $U(n+2)$ is computed.

Therefore, although the system evolution is described at the event level, control updates and performance measurements are synchronized at the cycle level. This ensures consistency between the event-driven state updates, the cycle-based control inputs, and the physical signal timing implemented in the microscopic layer.

$$x_l(n+1) = x_l(n) - q_l^{out}(n) \cdot u_j(n) + q_l^{in}(n) \tag{1}$$

In Eq. (1), the control input $u_j(n)$ represents the effective green duration (seconds) assigned to direction j, including the associated transition intervals such as yellow times. Consequently, the red time for direction j is given by $CT - u_j(n)$. It is notable that although the model is event-based, the control input $u_j(n)$ represents the green time allocated over the corresponding signal cycle. Since $q_l^{out}(n)$ denotes the discharge rate (veh/s), the term $q_l^{out}(n) \cdot u_j(n)$ corresponds to the number of vehicles discharged during one cycle. The value of $u_j(n)$ is computed at the macroscopic decision instant corresponding to the end of cycle $[n-2, n]$ and is subsequently applied over the next cycle interval $[n, n+2]$. Within the microscopic layer, this cycle-level control input is implemented through fine-resolution signal timing and continuously enforced during the corresponding simulation steps. Fig. 1 illustrates the relevant timing and geometric parameters associated with Eq. (1) for a representative intersection approach.

The relationship between successive green durations is captured in Eq. (2), which relates $u_j(n+1)$ to its previous value $u_j(n)$ through the incremental change $\Delta u_j(n)$ applied in the preceding cycle, to ensure smooth changes in signal timings.

$$u_j(n+1) = u_j(n) + \Delta u_j(n) \tag{2}$$

Without loss of generality, and considering an arbitrary number of incoming streets and independent signalized directions, the event-based macroscopic state-space representation can be generalized. The resulting compact vector formulation, which stacks all approach-level states and control variables, is presented in Eq. (3).

$$X(n+1) = A \cdot X(n) + B(n) \cdot U(n) + q^{in}(n) \tag{3}$$

Here, $X(n) \in \mathbb{R}^N$ denotes the vector of queue lengths (in vehicles) at event n, where N is the number of approaches. The control input $U(n) \in \mathbb{R}^M$ represents the green time allocations (in seconds) for the M independently controlled signal phases. The input matrix $B(n) \in \mathbb{R}^{N\times M}$ maps control actions to queue variations and depends on the saturation flow rates. For $l = 1,\dots,N$ streets and $j = 1,\dots,M$ independent directions, we have:

$$A = \begin{bmatrix} 1 & 0 & \cdots & 0 \\ 0 & 1 & \cdots & 0 \\ \vdots & \vdots & \ddots & \vdots \\ 0 & 0 & \cdots & 1 \end{bmatrix}_{N\times N} = I_N, \quad B(n) \in \mathbb{R}^{N\times M} \tag{4}$$

$$X(n) = \begin{bmatrix} x_1(n) \\ \vdots \\ x_N(n) \end{bmatrix}_{N\times 1}, \quad q^{\text{in}}(n) = \begin{bmatrix} q_1^{\text{in}}(n) \\ \vdots \\ q_N^{\text{in}}(n) \end{bmatrix}_{N\times 1} \tag{5}$$

$$U(n) = \begin{bmatrix} u_1(n) \\ \vdots \\ u_M(n) \end{bmatrix}_{M\times 1}, \quad \sum_{j=1}^{M} u_j(n) = CT \tag{6}$$

where:

$$[B(n)]_{lj} = \begin{cases} -q_l^{\text{out}}(n), & \text{if street } l \text{ is actuated by phase } j, \\ 0, & \text{otherwise.} \end{cases} \tag{7}$$

Thus, the matrix $B(n)$ has units of veh/s, ensuring that $B(n)\cdot U(n)$ yields vehicle counts consistent with the state definition. From a practical standpoint, several physical and operational constraints must be considered at the macroscopic level. Street capacities impose upper bounds on vehicle accumulations, green durations are restricted by safety and coordination requirements, and variations in green time allocations must be limited to avoid abrupt or oscillatory control actions. These considerations give rise to a set of constraints that are explicitly enforced in the macroscopic control formulation. It is important to emphasize that the elements of $B(n)$ are not fixed parameters but are directly influenced by microscopic traffic conditions. In particular, the effective discharge rates $q_l^{\text{out}}(n)$ depend on vehicle-level dynamics such as car-following behavior, CAV penetration rate, and platoon formation.

For instance, the presence of CAVs operating in coordinated platoons reduces inter-vehicle headways and increases saturation flow rates, which leads to larger values of $q_l^{\text{out}}(n)$. Conversely, heterogeneous traffic with lower CAV penetration results in more conservative discharge behavior. Therefore, variations in microscopic traffic composition and behavior are reflected in the macroscopic model through the time-varying matrix $B(n)$.

$$0 \le x_l(n) \le x_{\max}, \tag{8}$$

$$u_{\min} \le u_j(n) \le u_{\max}, \tag{9}$$

$$\Delta u_{\min} \le \Delta u_j(n) \le \Delta u_{\max} \tag{10}$$

At the network scale, intersections operate in a decentralized manner and may adopt different green and red allocations within each cycle. Nevertheless, macroscopic decision updates are synchronized at the end of every cycle of duration CT. Specifically, after the two events defining the interval $[n, n+2]$, vehicle accumulations $x_l(n)$ are measured simultaneously across all intersections, and the corresponding green time decisions $u_j(n)$ for the next cycle are computed in parallel. This procedure ensures consistent application of Eq. (3) at the macroscopic decision instants, even though intermediate phase transitions are not globally aligned.

It is important to emphasize that the event-based state update and the cycle-based control application are fully aligned through this mechanism. While intermediate event transitions capture the switching behavior of signal phases, the aggregated state variation over two consecutive events corresponds exactly to one full control cycle governed by $U(n)$. As a result, the macroscopic model preserves physical consistency with the implemented signal timing and avoids any mismatch between state evolution and control execution.

2.2. Microscopic level

At the microscopic level, vehicle dynamics are described using a discrete-time state-space model similar to that proposed in [49]. For an individual vehicle indexed by i, the state variables at time step k include the position $p_i(k)$, velocity $V_i(k)$, and acceleration $a_i(k)$. The control input applied to the vehicle is denoted by $U_i'(k)$, while $W_i'(k)$ represents unmodeled disturbances. Owing to the fine-grained nature of vehicle motion, the microscopic sampling interval must be chosen sufficiently small.

$$X_i'(k+1) = A' \cdot X_i'(k) + B' \cdot \left(U'_i(k) + W_i'(k)\right) \tag{11}$$

In Eq. (11),

$$X_i'(k) = \begin{bmatrix} p_i(k) \\ V_i(k) \\ a_i(k) \end{bmatrix}, \quad A' = \begin{bmatrix} 1 & T_s & 0 \\ 0 & 1 & T_s \\ 0 & 0 & e^{-T_s/T_d} \end{bmatrix}, \tag{12}$$

$$B' = \begin{bmatrix} 0 \\ 0 \\ 1 - e^{-T_s/T_d} \end{bmatrix}, \quad \left\| W_i'(k) \right\|_2 \in [0, \infty) \tag{13}$$

In this formulation, the parameter T_d represents the inertial time constant of the vehicle, characterizing the delay between a commanded acceleration and its actual realization. The variable T_s denotes the microscopic control and sampling interval, indexed by $k = 1,2,3,\dots$. The exponential term e^{-T_s/T_d} models a first-order lag response, ensuring gradual adaptation of acceleration, while the complementary term $1 - e^{-T_s/T_d}$ captures the proportion of the new control command applied within each sampling step. This structure prevents unrealistically abrupt acceleration changes and reflects the physical behavior of real vehicles.

The discrete-time interval $[k, k+1]T_s$ describes the evolution of the microscopic state according to Eq. (11). Since vehicle speed and acceleration are inherently bounded by physical limitations and safety considerations, appropriate constraints are imposed on these variables within the microscopic model to ensure feasible and realistic behavior.

$$0 \le V_i(k) \le V_{\max}, \tag{14}$$

$$-a_{deceleration}^{max} \le a_i(k) \le a_{acceleration}^{max} \tag{15}$$

In addition to the state-space vehicle model, the microscopic layer incorporates signal-aware motion planning and platoon coordination mechanisms. To this end, several auxiliary variables are defined to characterize the interaction between macroscopic and microscopic layers:

- $Dist_{i,j}(t)$: longitudinal distance of vehicle i to the stop line at time t in direction j,
- $RGT_j(t)$: remaining green time of the current phase in direction j,
- $TG_j(t)$: time until the next green phase in direction j,
- $SafeGap$: minimum safe distance to the preceding vehicle,
- $MaxGap$: maximum distance for being a member of platoon.

Based on these variables, a reachable distance under maximum allowable speed is defined as:

$$CD_j(t) = V_{\max} \cdot RGT_j(t) \tag{16}$$

If $Dist_{i,j}(t) \leq CD_j(t)$, the vehicle can safely pass the intersection within the current green phase; otherwise, it must adapt its speed to the next cycle. Accordingly, a recommended speed is computed as:

$$V_{i,\text{recommended}}(t) = \frac{Dist_{i,j}(t)}{TG_j(t)} \tag{17}$$

These signal-aware speed adjustments enable coordinated platoon formation and smoother approach behavior, reducing stop-and-go dynamics and improving discharge efficiency. Without loss of generality and for better clarification, the proposed control framework is demonstrated on a single signalized intersection with four incoming approaches and two independent directions, namely north–south and east–west. Each direction is assigned a dedicated green interval. Under this configuration, the general macroscopic state-space model in Eq. (3) reduces to the explicit form given in Eqs. (18)–(20).

$$X(n) = \begin{bmatrix} x_1(n) \\ x_2(n) \\ x_3(n) \\ x_4(n) \end{bmatrix}, \quad A = \begin{bmatrix} 1 & 0 & 0 & 0 \\ 0 & 1 & 0 & 0 \\ 0 & 0 & 1 & 0 \\ 0 & 0 & 0 & 1 \end{bmatrix} = I_4, \tag{18}$$

$$B(n) = \begin{bmatrix} -q_1^{\text{out}}(n) & 0 \\ 0 & -q_2^{\text{out}}(n) \\ -q_3^{\text{out}}(n) & 0 \\ 0 & -q_4^{\text{out}}(n) \end{bmatrix}, \quad q^{\text{in}}(n) = \begin{bmatrix} q_1^{\text{in}}(n) \\ q_2^{\text{in}}(n) \\ q_3^{\text{in}}(n) \\ q_4^{\text{in}}(n) \end{bmatrix} \tag{19}$$

$$U(n) = \begin{bmatrix} u_1(n) \\ u_2(n) \end{bmatrix}, \qquad u_1(n) + u_2(n) = CT \tag{20}$$

When a particular direction is assigned a red signal, the corresponding departure flows vanish, implying $q_i^{out}(n) = 0$ for the affected approaches $i = 1, \dots, 4$. Given a fixed cycle time CT, each cycle allocates two distinct green intervals to the competing directions, whose durations collectively sum to the cycle length.

The impact of microscopic control actions propagates back to the macroscopic level through aggregated traffic quantities. Specifically, the effective discharge flow $q_l^{\text{out}}(n)$ and the measured state $x_l(n)$ are computed from microscopic observations over each cycle. As a result, improvements in vehicle coordination, platoon stability, and speed harmonization directly translate into enhanced macroscopic performance, including reduced queue lengths and increased throughput. This establishes a closed-loop coupling in which macroscopic decisions influence microscopic behavior, and microscopic dynamics, in turn, reshape the macroscopic model parameters and state evolution.

Although a direct integration of the macroscopic and microscopic models into a single unified formulation is not feasible due to their different time representations, the proposed framework ensures tight coupling through systematic bidirectional information exchange. The macroscopic layer provides cycle-level control inputs, while the microscopic layer refines these decisions through vehicle-level execution and feeds back aggregated information that continuously updates the macroscopic state and model parameters. This interaction enables a coherent multi-scale control strategy rather than two independent models.

3. Adaptive-robust control synthesis

To ensure reliable and certifiable performance under the multiple sources of uncertainty that characterize real urban intersections, we develop a robust state-feedback regulator synthesized via LMIs. Traditional signal-control techniques often struggle to maintain performance when effective link discharge varies unpredictably, as highlighted in recent comprehensive reviews of tidal and urban traffic management [12]. In practice, this variability is commonly represented as uncertainty in saturation flow rates and has important operational consequences [4,5]. In addition to classical drivers of saturation-flow variability (vehicle mix, weather, and lane geometry), pedestrian–vehicle interactions can be a dominant and intermittent source of uncertainty: for example, configurations where right-turning vehicles share a green interval with crossing pedestrians (a practice observed in many European contexts) frequently produce blocking effects that reduce the realized discharge rate and introduce strong, time-varying capacity loss at the stop line. We therefore treat the effective saturation flow as a compound, time-varying quantity whose uncertainty arises from both vehicular and non-vehicular causes.

Against this backdrop, an LMI-based synthesis is attractive because it (i) yields convex, numerically tractable conditions for a Lyapunov certificate of exponential queue regulation, (ii) readily accommodates polytopic descriptions of input-matrix uncertainty and actuator constraints, and (iii) admits a computationally efficient trace-based surrogate objective compatible with semidefinite programming solvers, like as shown in [50]. In what follows, we first formalize the structured uncertainty model for the input mapping that captures extreme saturation-flow realizations and pedestrian-induced capacity reductions. Next, we present the implementable LMI conditions that guarantee one-step exponential decrease of a quadratic Lyapunov function across all uncertainty vertices, and finally, we describe a convex synthesis problem that trades off the Lyapunov shape and feedback gain magnitude via trace penalties, and all of these make the method suitable for decentralized, real-time operation in mixed CAV/HDV traffic.

3.1. Uncertainty description and LMI-based robust feedback

This formulation enables the application of LMI techniques to ensure the closed-loop stability for all admissible $B(n)$. In particular, the LMI condition guarantees that the closed-loop system remains stable under any saturation flow rate realization within the defined convex set. We seek a static matrix gain $K \in \mathbb{R}^{M \times N}$ such that:

$$U(n) = -KX(n), \tag{21}$$

$$X(n+1) = (I_N - B(n)K)X(n) + q^{in}(n). \tag{22}$$

It is important to note that the closed-loop system in Eq. (22) is non-homogeneous due to the presence of the exogenous inflow term $q^{in}(n)$. In this work, $q^{in}(n)$ is interpreted as a bounded disturbance, i.e.,

$$\|q^{in}(n)\| \leq \bar{q}, \quad \forall n, \tag{23}$$

for some finite constant $\bar{q} > 0$. Therefore, the stability analysis must be understood in the sense of disturbed systems rather than purely autonomous dynamics.

The entries of $B(n)$ are directly related to the saturation flow rates:

$$q_l^{\text{out}} = s_l, \qquad s_l^{\text{nom}} = 0.5 \text{ veh/s} = 1800 \text{ veh/h}. \tag{24}$$

So based on the discharge rate defined in Eq. (24), the total discharged vehicles over a green interval is given by $s_l \cdot u_j(n)$. The nominal value of s_l is based on ideal conditions in classical models [51,52]. To account for modeling variability, we represent uncertainty in the saturation flows by percentage bounds. For a given uncertainty level $\delta \in [0,1)$ we assume

$$s_l \in \left[(1-\delta)s_l^{\text{nom}},\ (1+\delta)s_l^{\text{nom}}\right]. \tag{25}$$

For synthesis, we collect extreme combinations of the per approach discharge into a small vertex set $\{B_i\}_{i=1}^N$ and model the true mapping as a convex combination

$$B(n) \in \text{conv}\{B_1, B_2, \dots, B_N\}, \tag{26}$$

$$B(n) = \sum_{i=1}^{N} \alpha_i B_i, \ \sum_i \alpha_i = 1, \ \alpha_i \geq 0. \tag{27}$$

A typical choice for the vertices is to set each B_i to the matrix corresponding to one extreme allocation of $(1 \pm \delta)s_l^{\text{nom}}T$ across approaches; this structured polytopic representation is widely used in robust traffic control since it yields tractable LMI conditions while capturing the dominant variability in effective discharge rates.

To fulfill stability, we seek a quadratic Lyapunov function $V(X) = X^\top P X$ with $P \succ 0$ that certifies uniform exponential decay of the closed loop for every admissible vertex B_i [53]. Exponential decrease at rate $\Lambda > 0$ is enforced by requiring the one step bound

$$V\left(X(n+1)\right) \le e^{-2\Lambda} V\left(X(n)\right), \quad \forall n \ge 0. \tag{28}$$

For the homogeneous closed-loop system (i.e., $q^{in}(n) = 0$), this condition guarantees exponential stability [54,55]. In the presence of bounded inflows, the same Lyapunov function can be used to establish a practical stability property, ensuring that the state remains ultimately bounded within a neighborhood whose size depends on the disturbance magnitude $\bar{q}$. Substituting $X(n+1) = (I_N - B_i K)X(n)$ and applying the Schur complement [56] yields the equivalent matrix inequality, valid for each vertex B_i:

$$\begin{bmatrix} e^{-2\Lambda} P & (I_N - B_i K)^\top P \\ P(I_N - B_i K) & P \end{bmatrix} \ge 0. \tag{29}$$

Under the bounded disturbance assumption, standard Lyapunov arguments imply that the closed-loop system satisfies an input-to-state practical stability property. In particular, there exist class $\mathcal{K}$ functions $\eta(\cdot)$ and $\gamma(\cdot)$ such that:

$$\|X(n)\| \le \eta(\|X(0)\|)e^{-\Lambda n} + \gamma(\bar{q}), \tag{30}$$

which guarantees that all trajectories remain bounded and converge to a disturbance-dependent invariant set.

To obtain a convex implementable form, we apply the standard change of variables $\Gamma = KP$, so that $K = \Gamma P^{-1}$. With this substitution Eq. (29) can be written as the LMI:

$$\begin{bmatrix} e^{-2\Lambda} P & (P - B_i \Gamma)^\top \\ P - B_i \Gamma & P \end{bmatrix} \ge 0, \qquad P \succ \epsilon I, \tag{31}$$

for $i = 1, \dots, N$. Condition (31) is the working robustness certificate used in our synthesis. The equivalence between the quadratic decrease requirement (28) and the LMI representation (31) follows by the Schur complement argument and is standard in the robust control literature; concise LMI reformulations for constrained and uncertain systems appear in [50]. Enforcing (31) for every vertex yields a convex feasible set in the decision variables (P, Γ, Λ). To produce a practically useful feedback gain, we solve the following SDP, which trades off a surrogate of state magnitude against feedback aggressiveness:

$$\begin{aligned} &\min_{P>0,\Gamma,\Lambda>0} \quad \operatorname{trace}(QP) + \operatorname{trace}(R\Gamma\Gamma^\top) \\ &\text{subject to} \quad P \ge \epsilon I, \\ &\begin{bmatrix} e^{-2\Lambda} P & (P - B_i \Gamma)^\top \\ P - B_i \Gamma & P \end{bmatrix} \ge 0, \quad i = 1, \dots, N \end{aligned} \tag{32}$$

After solving (32) the feedback gain is recovered as $K = \Gamma P^{-1}$. The trace terms are convex surrogates that make the problem SDP tractable while capturing the design intent: $\operatorname{trace}(QP)$ encourages smaller Lyapunov level sets in directions emphasized by Q, and $\operatorname{trace}(R\Gamma\Gamma^\top)$ penalizes large auxiliary variables, indirectly limiting the magnitude of the recovered gain. The choice of Q and R follows standard engineering tuning: Q encodes queue priorities and R bounds the admissible green time variations.

To complement the LMI-certified feedback and to avoid sustained accumulation of measurable short-horizon inflows $q^{in}(n)$, in the next subsection, we introduce a feedforward disturbance-rejection block together with an adaptive operational layer that conditions online re-synthesis on identification confidence and compute budget.

3.2. Adaptive operational layer and feedforward disturbance rejection

This subsection presents an operational layer that (i) estimates short-horizon, measurable inflows and input mappings from recent cycle data, (ii) computes a feedforward action to proactively counter predictable arrivals, and (iii) conditionally triggers online LMI re-synthesis when identification confidence and computational resources permit. The feedforward block consumes near-term inflow and upstream indicators to reduce transient queue growth, thereby decreasing the performance demands placed on the robust feedback adaptation loop. When re-synthesis is infeasible or rejected, a numerically stable LQR fallback is used to guarantee continuous and safe operation.

The adaptive layer is indirect adaptive (identify-then-control), i.e., at each cycle the controller attempts to estimate $B(n)$ from recent cycle data and, when confidence and compute budget permit, re-synthesizes a gain $K(n)$ via a convex LMI that certifies local exponential decrease of a quadratic Lyapunov function. It is important to emphasize that the above stability guarantee applies specifically to the state-feedback component derived from the LMI-based synthesis under polytopic uncertainty. The complete control architecture, however, incorporates additional elements, including feedforward disturbance compensation, online identification of the input matrix, gain updating, actuator saturation constraints, and an LQR fallback mechanism.

These elements are not explicitly covered by the theoretical LMI framework. Therefore, while the feedback component admits formal stability guarantees, the stability of the overall closed-loop system is not established analytically in this work. When identification is unreliable or the LMI solver fails (or compute budget is exceeded) the adaptive layer falls back to a numerically-robust LQR gain computed online from a nominal B_{nom}. A disturbance feedforward term, computed from measured inflows, reduces transient queue growth and alleviates performance pressure on feedback adaptation. The design balances performance vs. guaranteed stability and real-time tractability.

Recall the linearized dynamics:

$$\Delta X(k) = X(k+1) - X(k), \tag{33}$$

where we have

$$\Delta X(k) = Bu(k) + \Delta q(k), \tag{34}$$

that represents the net change in queue lengths under control inputs and inflow variations, where $\Delta q(k)$ represents the variation in exogenous inflows, i.e.:

$$\Delta q(k) := q^{in}(k+1) - q^{in}(k), \tag{35}$$

which is treated as an additive disturbance in the identification step. Let

$$\mathcal{D}_n = \{(u(k), \Delta X(k))\}_{k=n-W}^{n} \tag{36}$$

be the dataset of the recent W cycles. We construct the regressor matrix $\boldsymbol{\Psi}_n \in \mathbb{R}^{W\times M}$ (inputs) and the output matrix $\Delta\mathbf{X}_n \in \mathbb{R}^{W\times N}$ (state variations):

$$\boldsymbol{\Psi}_n := \begin{bmatrix} u(n-W) \\ \vdots \\ u(n-1) \end{bmatrix} \in \mathbb{R}^{W\times M}, \tag{37}$$

$$\Delta\mathbf{X}_n := \begin{bmatrix} (X(n-W+1) - X(n-W))^\top \\ \vdots \\ (X(n) - X(n-1))^\top \end{bmatrix} \in \mathbb{R}^{W\times N}. \tag{38}$$

We employ Tikhonov (ridge) regularization to stabilize the least-squares inversion when the normal matrix $\boldsymbol{\Psi}_n^\top \boldsymbol{\Psi}_n$ is ill-conditioned or near-singular. Concretely, a small scalar $\lambda \ge 0$ is added so that the optimal estimate $\hat{B}(n)$ is obtained by the least-squares solution:

$$\hat{B}(n)^\top = (\boldsymbol{\Psi}_n^\top \boldsymbol{\Psi}_n + \lambda I)^{-1} \boldsymbol{\Psi}_n^\top \Delta\mathbf{X}_n. \tag{39}$$

which trades small bias for numerical robustness [57]. Note that the measured state variation $\Delta X(k)$ implicitly contains the effect of inflow disturbances through the term $\Delta q(k)$. Under the assumption that $\Delta q(k)$ is bounded and exhibits weak correlation with the control input over the identification window, the least-squares estimate provides a consistent approximation of B. In practice, the use of a sliding window together with Tikhonov regularization mitigates the impact of such disturbances by averaging out high-frequency inflow variations. Although inflow is measurable, incorporating it explicitly into the regressor would increase model complexity and is therefore left for future work. The identification window length W should be chosen to ensure identifiability of the input map. In particular, for an unbiased least-squares estimate, the number of samples must satisfy $W \geq M$ and the regressor $\boldsymbol{\Psi}_n$ must have full column rank. Otherwise, Tikhonov regularization ($\lambda > 0$) provides a numerically stable but biased estimate. In practice, we select W to balance estimator variance, excitation requirements, and the desire for rapid adaptation. In addition to the window length requirement, reliable identification requires sufficient excitation of the input signal. In particular, the regressor matrix $\boldsymbol{\Psi}_n$ must satisfy a persistence of excitation condition. In practice, this is verified by ensuring that the smallest singular value of $\boldsymbol{\Psi}_n^\top \boldsymbol{\Psi}_n$ exceeds a prescribed threshold, i.e.:

$$\sigma_{\min}(\boldsymbol{\Psi}_n^\top \boldsymbol{\Psi}_n) \geq \epsilon_{\mathrm{pe}} > 0. \tag{40}$$

This condition guarantees that the input directions are sufficiently excited and that the estimated mapping $\hat{B}(n)$ is well-conditioned.

To ensure reliability of the estimated model, an acceptance test is applied before using $\hat{B}(n)$ for controller synthesis. The estimate is accepted only if all of the following conditions are satisfied:

- **Excitation condition:** $\sigma_{\min}(\boldsymbol{\Psi}_n^\top \boldsymbol{\Psi}_n) \geq \epsilon_{\mathrm{pe}}$,
- **Residual condition:** $\|\Delta \mathbf{X}_n - \boldsymbol{\Psi}_n \hat{B}(n)^\top\|_F \leq \epsilon_{\mathrm{res}}$,
- **Physical plausibility:** the entries of $\hat{B}(n)$ lie within the admissible bounds defined by Eq. (25).

If any of these conditions are violated, the identification result is rejected and not used for controller re-synthesis.

When identification is accepted, we compute a robust gain K by seeking a quadratic Lyapunov certificate that enforces exponential decrease of the closed-loop map. To ensure real-time feasibility, the LMI re-synthesis step is subject to a predefined computation time budget. If the solver does not return a feasible solution within this time limit, the update is aborted and the fallback controller is used.

The discrete-time algebraic Riccati equation (DARE) for the nominal system is:

$$\begin{aligned} P &= Q + A^\top P A \\ &- A^\top P B_{\mathrm{nom}} (R + B_{\mathrm{nom}}^\top P B_{\mathrm{nom}})^{-1} B_{\mathrm{nom}}^\top P A \end{aligned} \tag{41}$$

which can be solved by a standard DARE routine or by a small fixed-point iteration when desirable. The corresponding LQR gain is:

$$K_{\mathrm{LQR}} = \left(R + B_{\mathrm{nom}}^\top P B_{\mathrm{nom}}\right)^{-1} B_{\mathrm{nom}}^\top P A. \tag{42}$$

Choose $Q \succ 0$ and $R \succ 0$ to reflect the trade-off between queue regulation and control effort. The LQR fallback is computationally light, reliable, and guarantees a stabilizing action whenever the primary LMI re-synthesis is unavailable.

To reduce transient queue growth caused by measurable inflow surges, we treat the short-horizon inflows $q^{\mathrm{in}}(n)$ in Eq. (22) as (partially) predictable disturbances and add a feedforward term. The feedforward structure in Eq. (43) is motivated by a disturbance allocation perspective. Specifically, the inflow vector $q^{in}(n)$ represents the total incoming demand that must be served by the available green times within the cycle. Since the control input $U(n)$ directly determines the service capacity allocated to each direction, a natural feedforward strategy is to distribute the expected inflow proportionally across the controllable directions. To achieve this, the inflow vector is normalized to extract its directional distribution, and the matrix L_{ff} maps this normalized demand into admissible control actions. This results in a structured, yet computationally simple, feedforward term that anticipates demand imbalances and compensates them before they manifest as queue growth.

$$U_{ff}(n) = L_{ff} \frac{q^{in}(n)}{\mathbf{1}^\top q^{in}(n)} \tag{43}$$

where $L_{ff} \in \mathbb{R}^{M \times N}$ distributes total expected inflow to the M independent control directions according to approach priorities, $\mathbf{1} \in \mathbb{R}^N$ is the all-ones vector. The normalization makes the allocation scale-invariant (it prescribes a relative split of the inflow vector); absolute magnitudes can be tuned via the entries of L_{ff}. In this work, the matrix L_{ff} is selected based on a combination of structural considerations and empirical tuning. First, its structure reflects the mapping between incoming approaches and controllable signal phases. Second, the relative magnitudes of its entries are chosen to prioritize directions with higher capacity, e.g., approaches with a larger number of lanes are assigned higher feedforward gains.

The initial values of L_{ff} are determined through trial and error within a reasonable range of values, ensuring that the resulting control actions remain within admissible bounds and do not induce oscillatory behavior. This tuning process is guided by observed traffic performance metrics such as queue length, delay, and throughput under representative demand scenarios. The feedforward term $U_{ff}(n)$ is constructed directly from measurable inflow signals and can be interpreted as a disturbance compensation mechanism. Since $q^{in}(n)$ is assumed bounded, the feedforward input is also bounded, i.e.:

$$\|U_{ff}(n)\| \leq \bar{u}_{ff}. \tag{44}$$

Therefore, the inclusion of $U_{ff}(n)$ does not introduce instability, but instead reduces the effective disturbance seen by the feedback loop. It is important to note that the feedforward term does not affect the stability guarantees of the closed-loop system, which are ensured by the feedback component. In the case of mismatch or suboptimal tuning of L_{ff}, the feedforward action may lead to imperfect disturbance compensation; however, the feedback controller compensates for such discrepancies by correcting the resulting state deviations. Therefore, the role of the feedforward term is to improve transient performance rather than to guarantee stability, and the overall control scheme remains robust to inaccuracies in L_{ff}. Sensitivity to the choice of L_{ff} has been observed to be moderate in practice: overly large gains may lead to aggressive control actions and increased variability, while overly small gains reduce the effectiveness of disturbance anticipation. In our experiments, a bounded range of values provided consistent performance improvements across different traffic conditions.

The feedforward action is computed at each macroscopic decision step (at the end of each cycle) and clipped to actuator bounds before implementation. Combining feedback and feedforward yields the practical control law:

$$U(n) = U_{fb}(n) + U_{ff}(n) \ = \ -K(n)\, X(n) + U_{ff}(n), \tag{45}$$

where $K(n)$ denotes the (possibly time-varying) robust feedback gain from LMI synthesis (or K_{LQR} if the fallback is active). Substituting Eq. (45) into the system dynamics yields:

$$X(n+1) = (I_N - B(n)K(n))X(n) + B(n)U_{ff}(n) + q^{in}(n), \tag{46}$$

which can be interpreted as a disturbed closed-loop system with a combined disturbance term:

$$w(n) := B(n)U_{ff}(n) + q^{in}(n). \tag{47}$$

Since both $B(n)$ and $U_{ff}(n)$ are bounded, it follows that $w(n)$ is also bounded. Therefore, the previously established Lyapunov function ensures boundedness of the closed-loop trajectories in the presence of feedforward action. For implementation at the level of independent directions $j = 1, \ldots, M$, it is convenient to decompose the per-direction green-time increment into feedback and feedforward parts:

$$\Delta u_j(n) = \Delta u_{j,1}(n) + \Delta u_{j,2}(n), \tag{48}$$

Algorithm 1 Adaptive Identification and Control Update

```
Collect recent data D_n = {(u(k), ΔX(k))}_{k=n−W}^{n}
Construct regressor Ψ_n and output matrix ΔX_n
Compute B̂(n) via Eq. (39)
Evaluate excitation condition: σ_min(Ψ_n^⊤ Ψ_n) ≥ ϵ_pe
Compute residual: ‖ΔX_n − Ψ_n B̂(n)^⊤‖_F
if all acceptance criteria satisfied then
    Attempt LMI re-synthesis using B̂(n)
    if solver succeeds within time budget then
        Set K(n) = Γ P^{−1}
    else
        Set K(n) = K_LQR
    end if
else
    Set K(n) = K_LQR
end if
Compute feedforward input U_ff(n) via Eq. (43)
Compute control:
    U(n) = −K(n)X(n) + U_ff(n)
Apply projection:
    U(n) ← Π_U(U(n))
Update green times:
    u_j(n + 1) = u_j(n) + Δu_j(n)
```

$$\Delta u_{j,1}(n) = \left[-K(n)\, X(n)\right]_j, \tag{49}$$

$$\Delta u_{j,2}(n) = \left[U_{ff}(n)\right]_j, \tag{50}$$

and then set $u_j(n+1) = u_j(n)+\Delta u_j(n)$, with appropriate clipping to satisfy cycle constraints and physical bounds. In practice, actuator constraints impose bounds on admissible green times, leading to a clipped control input that can be expressed as:

$$U(n) = \Pi_{\mathcal{U}}\left(-K(n)X(n) + U_{ff}(n)\right), \tag{51}$$

where $\Pi_{\mathcal{U}}(\cdot)$ denotes projection onto the feasible set of control inputs defined by minimum/maximum green times and cycle-sum constraints. This results in a nonlinear, but bounded, control law. Since the projection operator is non-expansive and the feasible set $\mathcal{U}$ is compact, the resulting control input remains bounded. Under these conditions, the closed-loop system can still be interpreted as a disturbed system with bounded input, and the practical stability property is preserved.

Note that Eq. (45) and the per-direction decomposition in Eq. (48) are equivalent descriptions at different levels of abstraction. Eq. (45) expresses the control command as a vector-valued superposition (feedback plus feedforward), while Eq. (48) exposes the cycle-by-cycle allocation computed per independent direction, which is the quantity implemented in the actuator. This equivalence can also be interpreted from an incremental viewpoint. Since the control implementation starts from an initial green-time vector $U(0)$ at the beginning of the simulation or deployment, both the feedback and feedforward gains act by adjusting the green times relative to the previous cycle. Accordingly, the control law does not prescribe absolute green durations at each step, but rather computes corrective increments that refine the previously applied signal plan based on the current state and anticipated inflows.

By summing two signals, i.e., robust feedback component (U_{fb}) and feedforward disturbance rejection (U_{ff}), the final control command effectively rejects predictable demand surges via the feedforward channel while maintaining robust stability margins via the feedback loop, as illustrated in the proposed control architecture in Fig. 2.

Regarding the scalability of our proposed decentralized controller, because each intersection computes its next green time independently at the end of each cycle, and these computations occur in parallel, the overall processing time grows essentially linearly with the number of intersections. This parallelization ensures the effective increase in computation time remains minimal even for large networks.

To address this limitation, we adopt an empirical stability validation approach. Specifically, the proposed controller is extensively evaluated through simulation across a wide range of operating conditions, including varying initial queue states, demand levels, CAV penetration rates, and uncertainty realizations. The results consistently show bounded queue evolution and stable system behavior under all tested scenarios. This provides strong empirical evidence supporting the practical stability and robustness of the overall control architecture, despite the absence of a unified analytical guarantee for the full closed-loop system.

4. Experimental results

We validate the proposed adaptive-robust control architecture using empirical traffic measurements collected at a busy signalized location in Tehran city during a representative peak-hour in July 2025. The dataset pertains to an arterial corridor containing two closely spaced signalized junctions; a map of the instrumented area is provided in Fig. 3. The inter-junction spacing of the two sites is approximately 500 m.

For the experiments reported here, we model the area as a two-node arterial network and concentrate the controller performance analysis on the central junction while treating the neighboring junction as a realistic boundary node that supplies inflow and absorbs outflow. It is worth noting that the simplified two-phase control structure adopted in this study (two independent directions) is primarily chosen to facilitate clear analysis and interpretation of the control performance. The proposed control framework, however, is not limited to this configuration.

In more general intersection settings, additional phases such as protected turning movements, pedestrian crossings, and clearance intervals (lost times) can be incorporated by augmenting the control input vector and appropriately redefining the phase structure. In such cases, the system matrices (in particular the input matrix $B(n)$) can be extended to capture the corresponding saturation flows and phase-specific constraints. From a control design perspective, the LMI-based synthesis and adaptive identification procedures remain applicable, as they naturally scale with the dimension of the system. Therefore, the proposed framework can be extended to realistic multi-phase intersections without fundamental modifications, at the cost of increased model dimensionality.

The simulation environment is developed using the SUMO package.[1] The microscopic simulations are conducted using the SUMO platform with standard modeling assumptions to ensure reproducibility and consistency:

- **Car-following and lane-changing models:** The default SUMO Krauss car-following model [48] is employed, which is widely used in traffic simulation studies. The model parameters, including acceleration, deceleration, minimum gap, desired time headway, and driver imperfection factor, are set to their default values as specified in the SUMO documentation. Lane-changing behavior is governed by the default SUMO lane-changing model without additional parameter tuning.
- **Traffic demand and turning movements:** Traffic demand and turning ratios are derived directly from empirical detector measurements collected at the study site during the peak-hour period. These measurements provide lane-level flow data, which are used to construct origin–destination movements and boundary inflows in the simulation.

[1] The SUMO parameter sets used in this study are available at: https://github.com/Arshia-Abdi/SUMO-Parameters-Set.git.

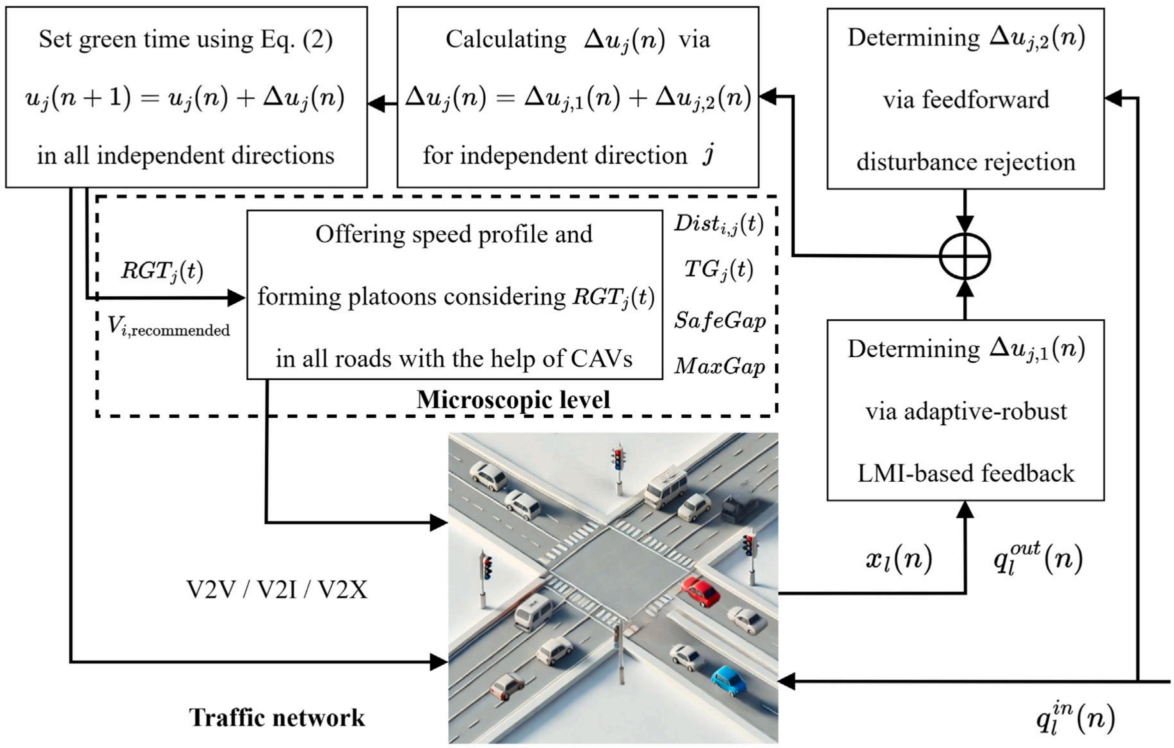

Fig. 2. Two-level adaptive-robust control architecture: LMI-based intersection-level feedback, feedforward disturbance rejection from short-horizon inflow estimates, and microscopic CAV-enabled platooning.

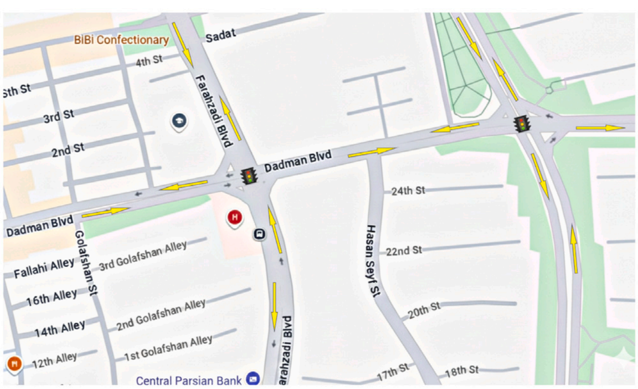

Fig. 3. The study area (35°45′57.5″N 51°21′43.4″E) and the instrumented approaches used in the experiments. The highlighted arrows indicate the primary approaches that were monitored and used to set boundary conditions in the simulations.

Table 1
Value of simulation parameters.

Parameter	Symbol and Value
Number of intersection approaches	$n = 4$
Number of independent directions	$m = 2$
Cycle time duration	$CT = 123$ s
Minimum green time duration	$u_{\min} = 40$ s
Maximum green time duration	$u_{\max} = 80$ s
Minimum per-cycle change	$\Delta u_{\min} = -10$ s
Maximum per-cycle change	$\Delta u_{\max} = 10$ s
Maximum allowable speed	$v_{\max} = 50$ km/h
Maximum acceleration	$a_{\mathrm{acc}}^{\max} = 2.5$ m/s^2
Maximum deceleration	$a_{\mathrm{dec}}^{\max} = 4.5$ m/s^2
Uncertainty level	$\delta = 0.2$ (20%)
LMI decay rate factor	$\Lambda \approx 0.005$
LQR weight matrices	$Q = I_4, R = 0.1 I_2$
Initial green time control input	$U(0) = \begin{bmatrix} 60 \\ 60 \end{bmatrix}$ s
Initial feedforward gain	$L_{ff} = \begin{bmatrix} -5 & 0 & -5 & 0 \\ 0 & -2.5 & 0 & -2.5 \end{bmatrix}$

- **Signal timing and phase structure:** The signal phase configuration, number of phases, and operational constraints are based on field observations and information obtained from local traffic operators. These configurations are replicated in the SUMO environment to ensure realistic representation of the intersection control logic.
- **Calibration and validation:** Rather than performing a full microscopic trajectory calibration, the simulation is designed to reproduce key macroscopic traffic characteristics, including queue formation, discharge rates, and throughput. The use of measured inflow data ensures consistency between simulated and observed traffic patterns.
- **Saturation flow assumption:** The nominal saturation flow rate is set to 0.5 veh/s (1800 veh/h), which is matched with Tehran traffic situation, and also it is a widely accepted reference value in urban traffic engineering. So, while local driving behavior and geometric conditions may introduce deviations, this value serves as a reasonable baseline.

The specific configuration parameters and controller settings employed in the simulation are summarized in Table 1. The empirical site departs from idealized, symmetric testbeds in several important ways. Measured inflow rates are heterogeneous across approaches, and lane configurations differ between directions: for instance, the east–west approaches at the Dadman–Farahzadi junction feature four lanes, while the north–south approaches are three-lane links. Furthermore, a geometric discontinuity exists: there is no direct east-to-north turning movement (Dadman East → Farahzadi North). These asymmetries and the uneven distribution of demand produce realistic propagation and

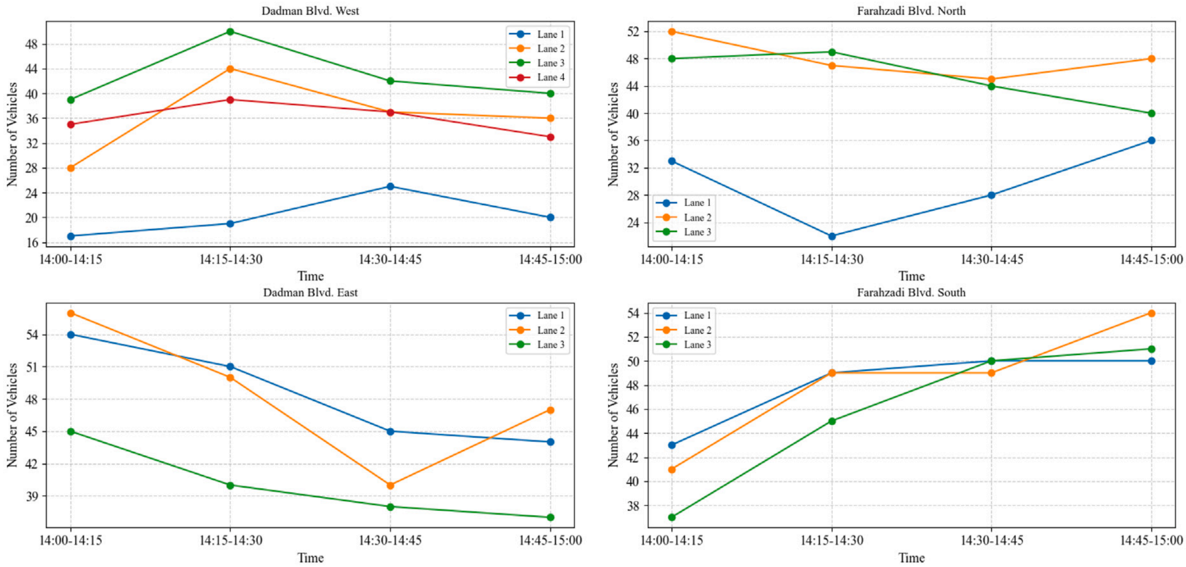

Fig. 4. An example of lane-by-lane measured traffic volumes at the Dadman–Farahzadi junction during the representative peak window (14:00–15:00, July 2025). These empirical traces were employed both to feed the microscopic SUMO simulations and to set macroscopic boundary conditions in the state-space experiments.

spillback phenomena, which are retained by using the observed outflows from the upstream junction as the inflows for the downstream node in our arterial model.

Fig. 4 reports an exemplar subdivision of the observed traffic volumes across the instrumented approaches during the analyzed hour (14:00–15:00). The lane-level flow traces shown in the figure were used in two complementary ways: (i) as boundary inputs to the microscopic SUMO experiments that evaluate vehicle-level interactions and CAV/platoon behavior; and (ii) to specify macroscopic boundary conditions and initial states in the discrete-event state-space simulations used for control synthesis and performance assessment. All controller comparisons and performance metrics presented below (queue lengths, throughput, etc.) refer to the central intersection; the neighboring junction provides realistic dynamic inflows that allow queue spillback and network effects to arise naturally. These empirical measurements are directly used to construct the simulation inputs, including demand profiles and turning movements, ensuring consistency between the real-world observations and the simulated environment. It is important to note that the objective of the simulation setup is to achieve realistic macroscopic traffic behavior rather than exact microscopic trajectory matching, which is consistent with the control-oriented focus of this study.

To demonstrate the effectiveness and robustness of the proposed Two-Level Adaptive-Robust Traffic Signal Control, comprehensive simulations were conducted using the SUMO microsimulation environment. In addition to performance evaluation, the simulation campaign also serves as an empirical stability validation of the proposed control architecture. A wide range of scenarios is considered, including different CAV penetration levels, uncertainty realizations, and initial conditions, to systematically assess the closed-loop behavior. Across all tested cases, the system exhibits stable queue dynamics with no evidence of divergence or instability, supporting the practical reliability of the proposed method. The simulations evaluate the performance of the controller under mixed traffic conditions with varying CAV penetration rates (0%, 25%, 50%, 75%, and 100%).

In practical deployments, the CAV penetration rate can be estimated using a combination of vehicle-to-infrastructure (V2I) communication and infrastructure-based sensing technologies. Connected vehicles can directly communicate their status via roadside units (RSUs), while conventional vehicles can be inferred through loop detectors, cameras, or radar sensors. It is important to note that such estimates may be affected by noise, latency, or partial observability. To address this, the proposed control framework incorporates a reliability-aware adaptation mechanism. In particular, the estimated penetration rate is only used to adjust adaptive components when the underlying data satisfies predefined confidence conditions, such as consistency of measurements over multiple cycles and sufficient data availability. If these conditions are not met (e.g., due to missing data, high variability, or sensor degradation), the controller automatically disables the adaptation logic and switches to a conservative fallback mode based on LQR control. This ensures that the system maintains stable and safe operation independently of the accuracy of the penetration rate estimation. Therefore, the robustness of the control architecture does not rely on precise estimation of CAV penetration, and the adaptation mechanism is designed to gracefully degrade in the presence of unreliable or incomplete data.

Figs. 5 and 6 show two samples of the simulation results for the Adaptive-Robust LMI-based control (ARLMI) scenario under nominal and uncertain conditions, respectively. These plots depict the dynamic green time allocations, vehicle trajectories for both CAVs and HDVs, and the temporal evolution of vehicle queues across the intersection approaches.

The proposed **ARLMI** method, is benchmarked against four distinct control strategies to validate its superiority in terms of traffic efficiency and environmental impact:

- **Fixed-Time (FT):** A classical pre-timed signal plan optimized for historical average traffic data.
- **Fixed-Time + Platooning (FT+PL):** The FT strategy augmented with a platooning algorithm for CAVs to enhance discharge rates.
- **SUMO Gap-Actuated Adaptive Control (SGAAC):** The built-in actuated traffic control logic provided by SUMO, which extends or recalls phases based on time gaps detected by sensors [48].
- **Zero-Shot LLM Advisor (ZSLLM):** An emerging AI-based approach utilizing a large language model to generate control decisions. The LLM is employed in a zero-shot manner, meaning that no task-specific training or fine-tuning is performed for the traffic control problem. Instead, control actions are generated through structured prompts that encode the current traffic conditions, including queue lengths and recent control actions. The objective of including this scenario is not to develop or optimize an AI-based controller, but rather to provide a qualitative benchmark illustrating the trade-offs between advanced AI-driven decision-making

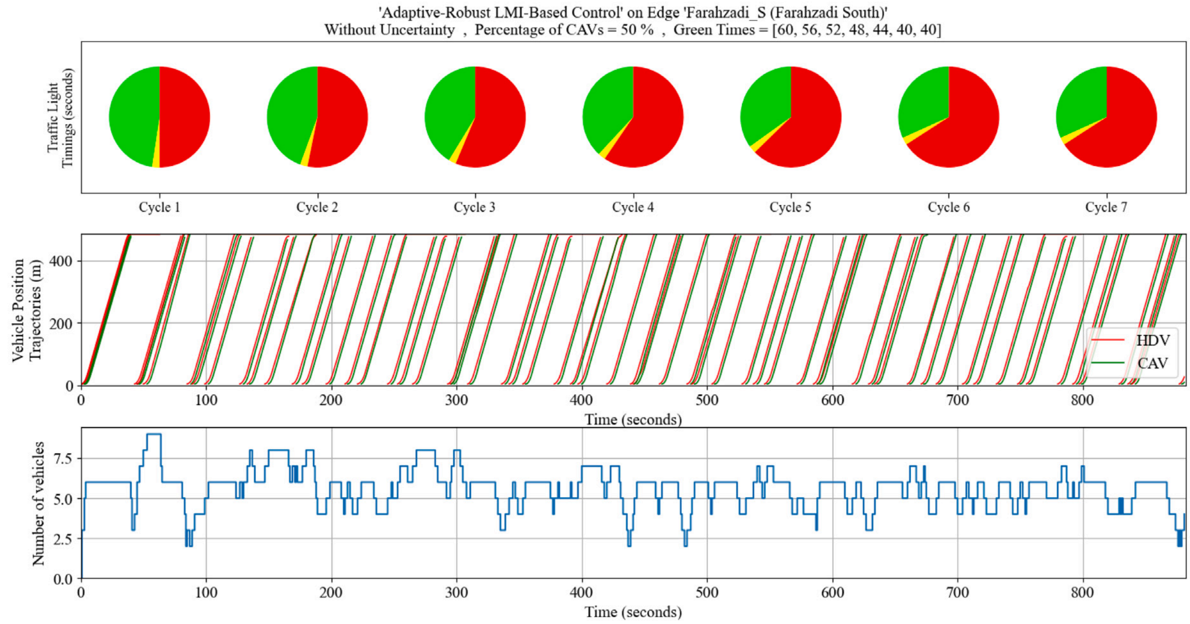

Fig. 5. Illustrative results of the proposed ARLMI scenario for real data of Tehran city, with CAV penetration rate = 50% and without uncertainty.

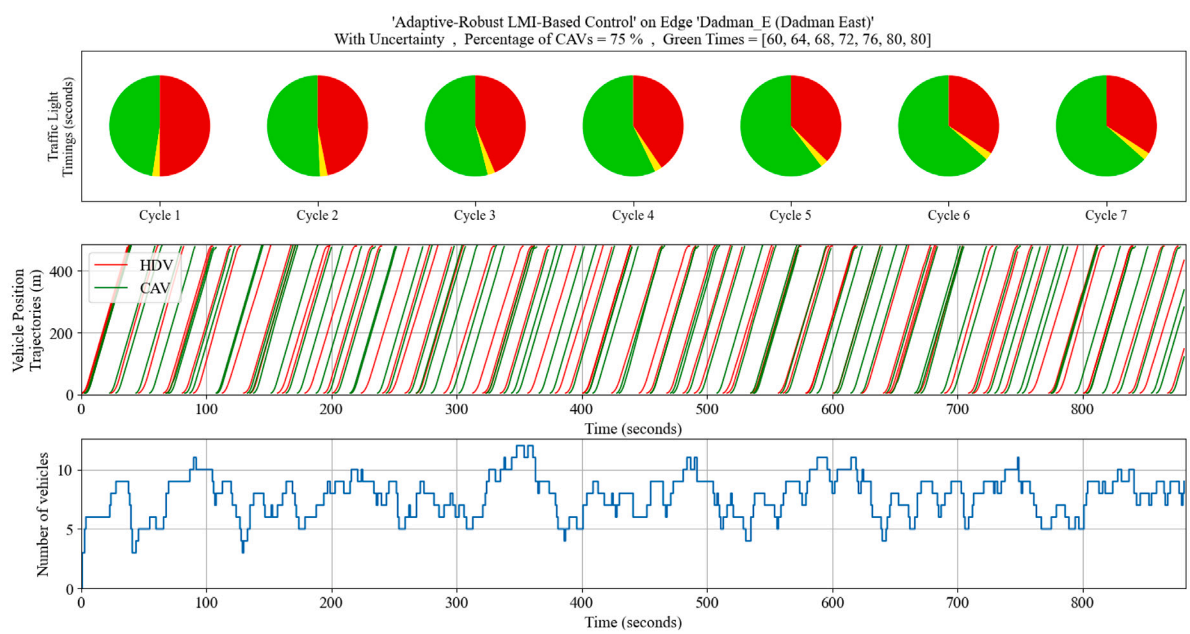

Fig. 6. Illustrative results of the proposed ARLMI scenario for real data of Tehran city, with CAV penetration rate = 75% and in the presence of uncertainty.

and real-time feasibility. The prompt design and interaction protocol are kept intentionally simple to reflect a generic deployment setting without problem-specific optimization. It should be noted that the performance of this approach depends on external inference resources and may be affected by communication latency and model response time. Therefore, this method is primarily included to highlight computational and practical limitations of LLM-based control in real-time traffic applications, rather than as a fully optimized competing strategy.

- **Adaptive MPC (AMPC)**: A data-driven adaptive model predictive control strategy in which the input matrix is recursively estimated online using recent measurements of the system state and applied control inputs. At each cycle, a finite-horizon quadratic optimization problem is solved to regulate queue lengths by adjusting green times subject to operational constraints. Unlike the proposed **ARLMI**, this approach does not explicitly account for parametric uncertainty in a robust manner, but instead relies on online model adaptation to capture time-varying traffic dynamics. This benchmark is included to provide a comparison against a modern adaptive optimization-based control strategy widely used in traffic signal control.

It is worth noting that the selected benchmark strategies include both classical and adaptive traffic control approaches commonly used in practice. In particular, the inclusion of the **AMPC** scenario provides a representative comparison against optimization-based adaptive control methods, enabling a fair evaluation of the proposed **ARLMI** framework against state-of-the-art model-based strategies. The performance is evaluated using six key metrics:

- TTP: Total Throughput (veh)

Table 2
Comparison of calculating and processing time between the proposed Adaptive-Robust LMI-Based Control and Zero-Shot LLM Advisor. The LMI approach demonstrates superior real-time feasibility.

Control Scenario	Calculation and Processing Time (Seconds)						
	Cycle 1	Cycle 2	Cycle 3	Cycle 4	Cycle 5	Cycle 6	Mean
ARLMI	0.0059	0.000523	0.000601	0.000578	0.000787	0.001976	0.001728
ZSLLM	3.71	4.88	3.77	3.51	3.38	3.5	3.791667
ZSLLM (Think Mode)	9.26	14.87	10.71	7.33	7.01	7.98	9.526667

- TWT: Total Waiting Time (s)
- ATT: Average Travel Time (s)
- ALT: Average Loss Time (s)
- CO2: Total CO_2 Emission (mg)
- NOx: Total NO_x Emission (mg)

For improved readability, emission-related metrics may be presented in scaled units (e.g., $\times 10^6$ mg for CO_2 and $\times 10^4$ mg for NO_x) in some figures.

A critical requirement for urban traffic control is real-time feasibility. As suggested by recent trends, AI-based methods, such as LLMs, are powerful but often suffer from high computational latency. We compared the average calculation and processing time of the proposed **ARLMI** method against the **ZSLLM** advisor. All methods were executed on the same computational platform to ensure a fair comparison of processing times. The hardware configuration includes a standard desktop environment, and no method was given access to specialized acceleration (e.g., GPUs) beyond what is inherently required by the LLM inference process. This ensures that the reported computational times reflect practical deployment conditions.

As illustrated in Table 2, the proposed **ARLMI** synthesis offers a significantly lower computational burden compared to the LLM-based approach. While the **ZSLLM** suffers from inference latencies that may impede real-time actuation, the **ARLMI** optimization problem is convex and can be solved efficiently (in milliseconds), ensuring scalability for larger networks and guaranteeing that control actions are applied without delay. It is important to emphasize that the LLM-based method was not extensively tuned or optimized for this specific application. The goal of this comparison is not to achieve the best possible AI-based performance, but rather to provide a baseline illustration of the trade-offs between data-driven AI approaches and control-theoretic methods in terms of computational efficiency and real-time applicability. Furthermore, the performance of the **ZSLLM** is inherently tied to network stability and API communication speeds; thus, potential internet latency or server-side delays could further exacerbate its execution time. In contrast, the **ARLMI** framework operates locally with minimal computational requirements, providing a robust and reliable solution that maintains high-speed performance regardless of external communication constraints.

To thoroughly analyze the capability of the proposed controller, we consider two primary conditions regarding the saturation flow: (1) a nominal scenario without uncertainty, and (2) a worst-case perturbation to rigorously evaluate the controller's resilience. Specifically, the inflow rates for all horizontal links in the traffic network increase by 20% from their nominal values. Also a parametric uncertainty scenario in which the saturation flow rates are perturbed within ±20% bounds is considered, as detailed in Appendix. This level of uncertainty is selected based on empirical characteristics of the studied traffic network, which operates close to saturation during peak periods. Under such conditions, variability in driver behavior, vehicle interactions, and lane utilization can induce fluctuations in effective discharge rates of similar magnitude. Furthermore, selecting significantly larger uncertainty bounds (e.g., 40%–50%) would correspond to unrealistically severe traffic disruptions or poorly calibrated models, which are not consistent with the observed operating conditions of the studied network. Therefore, the chosen ±20% uncertainty level represents a balanced assumption that captures realistic variability while avoiding excessive conservatism in the control design. This deliberate stress test is designed to verify the proposed method's ability to maintain network stability and mitigate congestion even under significant demand surges and parameter variations.

In the scenario with nominal values and without uncertainty, the model parameters align perfectly with the simulation environment. Fig. 7 presents the comparative results across all metrics and penetration rates. Tables 3 and 4 present the absolute values and relative improvements with respect to the Fixed-Time baseline. The results show that both **ARLMI** and **AMPC** achieve substantial performance gains across all metrics and penetration levels, significantly outperforming classical and actuated control strategies.

At 50% CAV penetration, **ARLMI** reduces the Average Travel Time (ATT) by approximately 68.51%, while **AMPC** achieves a comparable reduction of 68.24%. Similarly, both methods yield significant reductions in emissions, with **ARLMI** and **AMPC** decreasing CO_2 emissions by 61.89% and 61.88%, respectively.

In terms of Average Loss Time (ALT), the proposed **ARLMI** consistently provides the best performance, achieving reductions exceeding 94% across most penetration levels, slightly outperforming **AMPC**. Moreover, while **SGAAC** and **FT+PL** improve traffic efficiency compared to **FT**, they remain inferior to both **AMPC** and **ARLMI**. Overall, the results indicate that while **AMPC** serves as a strong adaptive benchmark, the proposed **ARLMI** framework achieves the best overall balance between efficiency, emission reduction, and delay minimization (see Fig. 8).

In the scenario with uncertainty present, the main strength of the proposed control lies in its ability to handle uncertainties. As seen in Figs. 9 and 10, non-robust methods (like standard **FT** or even adaptive methods tuned for nominal models) may see performance degradation. To more clearly illustrate the relationship between CAV penetration and system performance, we provide an aggregated view of the performance metrics across penetration levels in Figs. 11 and 12. Unlike Figs. 7 and 9, which present multi-dimensional comparisons across control strategies, these figures isolate the effect of CAV penetration by directly comparing performance metrics as a function of penetration rate.

As observed in both figures, increasing the CAV penetration rate consistently improves all key performance indicators, including ATT, ALT, CO_2, and NO_x, under both nominal and uncertain conditions. This trend indicates that higher availability of connected vehicle data and actuation capabilities leads to more predictable and controllable traffic dynamics, thereby reducing the effective uncertainty in the system.

Tables 5 and 6 summarize the results under structured uncertainty. As expected, non-robust strategies exhibit noticeable performance degradation, while both **AMPC** and **ARLMI** maintain strong performance. At 0% CAV penetration, **ARLMI** reduces Total Waiting Time (TWT) by 78.31%, closely followed by **AMPC** with a reduction of 77.80%, whereas **SGAAC** achieves a lower reduction of 69.44%. Similar trends are observed across other metrics, where **AMPC** provides a competitive adaptive response but remains slightly inferior to **ARLMI**, particularly in minimizing delay and loss time.

In terms of throughput, both **AMPC** and **ARLMI** maintain high values, achieving over 215% improvement compared to **FT** at low CAV penetration rates. However, **ARLMI** demonstrates more consistent performance across all uncertainty realizations, highlighting the advantage of explicitly incorporating robustness in the control design. These results confirm that while adaptive strategies such as **AMPC** can partially compensate for model uncertainties, the proposed **ARLMI** framework provides enhanced robustness and stability under worst-case conditions.

It should be noted that, while the LMI-based synthesis provides formal guarantees for the feedback component, the overall system stability is supported through extensive simulation-based validation rather

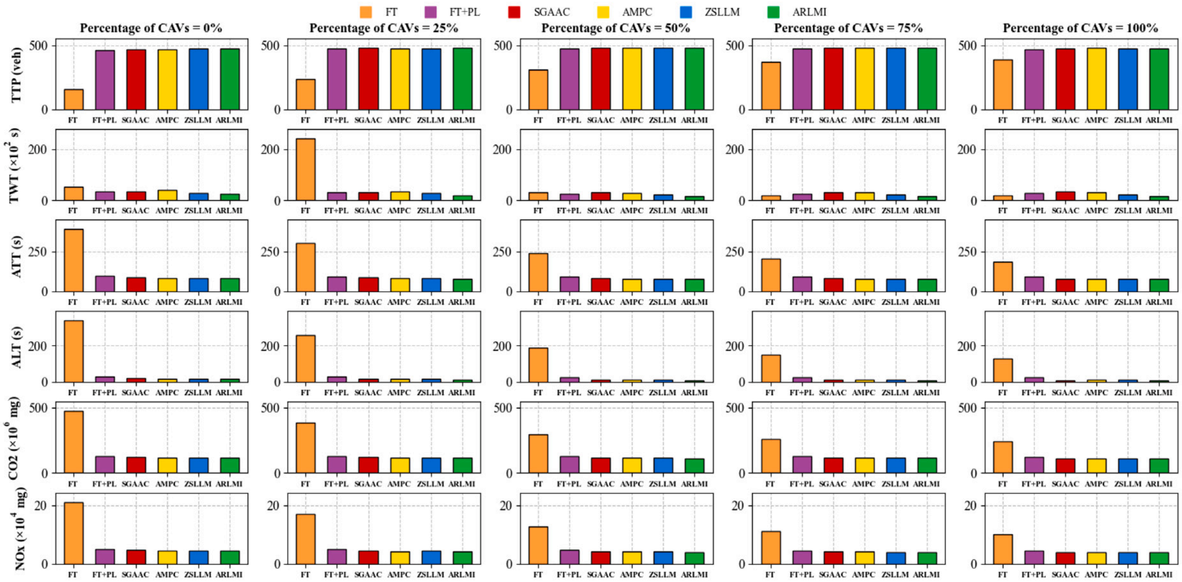

Fig. 7. Comparison between traffic control scenarios **Fixed-Time (FT), Fixed-Time + Platooning (FT+PL), SUMO Gap-Actuated Adaptive Control (SGAAC), Adaptive MPC (AMPC), Zero-Shot LLM Advisor (ZSLLM), Adaptive-Robust LMI-based control (ARLMI)** for different CAV penetration rates under nominal conditions (without uncertainty).

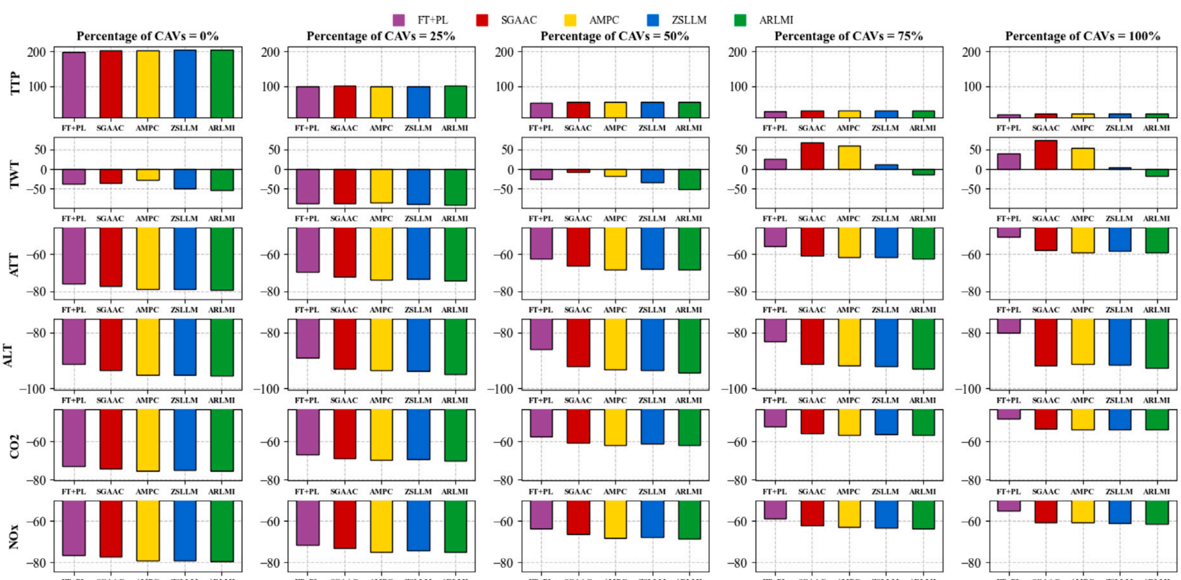

Fig. 8. Relative changes (%) of the different strategies compared to the **Fixed Time** scenario **Fixed-Time (FT), Fixed-Time + Platooning (FT+PL), SUMO Gap-Actuated Adaptive Control (SGAAC), Adaptive MPC (AMPC), Zero-Shot LLM Advisor (ZSLLM), Adaptive-Robust LMI-based control (ARLMI)** under nominal conditions (without uncertainty).

than a unified analytical proof. More specifically, stability is assessed through simulations over a wide range of operating conditions, including variations in initial queue lengths, demand patterns, uncertainty realizations, and CAV penetration levels. Across all tested scenarios, the closed-loop system consistently exhibits bounded queue evolution and absence of unstable behavior, providing strong empirical evidence of stability for the overall control architecture. This reflects the complexity of the full control architecture and aligns with common practice in large-scale traffic control systems. As mentioned before and to further enhance robustness under uncertain or unreliable measurements, a fallback mechanism is incorporated into the control architecture. In particular, when the online estimation or identification module fails to satisfy predefined confidence criteria (e.g., due to noisy or insufficient data), the controller switches to a conservative LQR-based control mode. This fallback strategy ensures that the system maintains stable and safe operation even under degraded sensing conditions, thereby preventing performance deterioration due to unreliable penetration rate estimation.

5. Discussion

The experimental evaluation confirms several core hypotheses motivating this work and provides practical insights into the strengths of the proposed **ARLMI** architecture.

First, the LMI-based state-feedback synthesis delivers formal, tractable stability certificates for the intersection-level store-and-forward model under structured polytopic uncertainty in the input matrix $B(n)$. By enforcing a one-step quadratic Lyapunov decrease

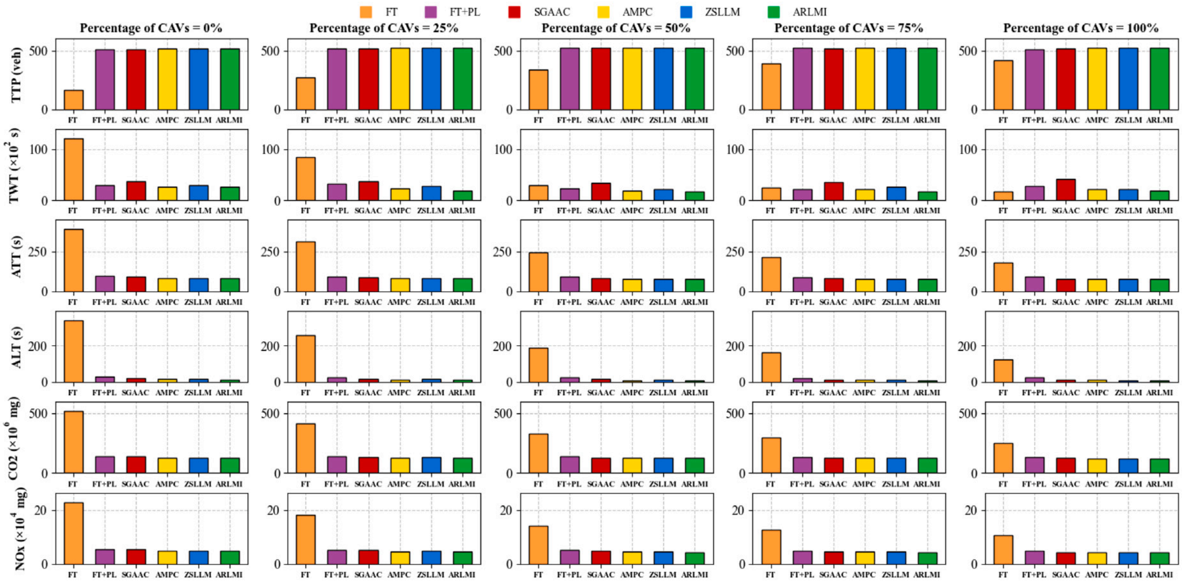

Fig. 9. Comparison between traffic control scenarios **Fixed-Time (FT), Fixed-Time + Platooning (FT+PL), SUMO Gap-Actuated Adaptive Control (SGAAC), Adaptive MPC (AMPC), Zero-Shot LLM Advisor (ZSLLM), Adaptive-Robust LMI-based control (ARLMI)** for different CAV penetration rates in presence of uncertainty.

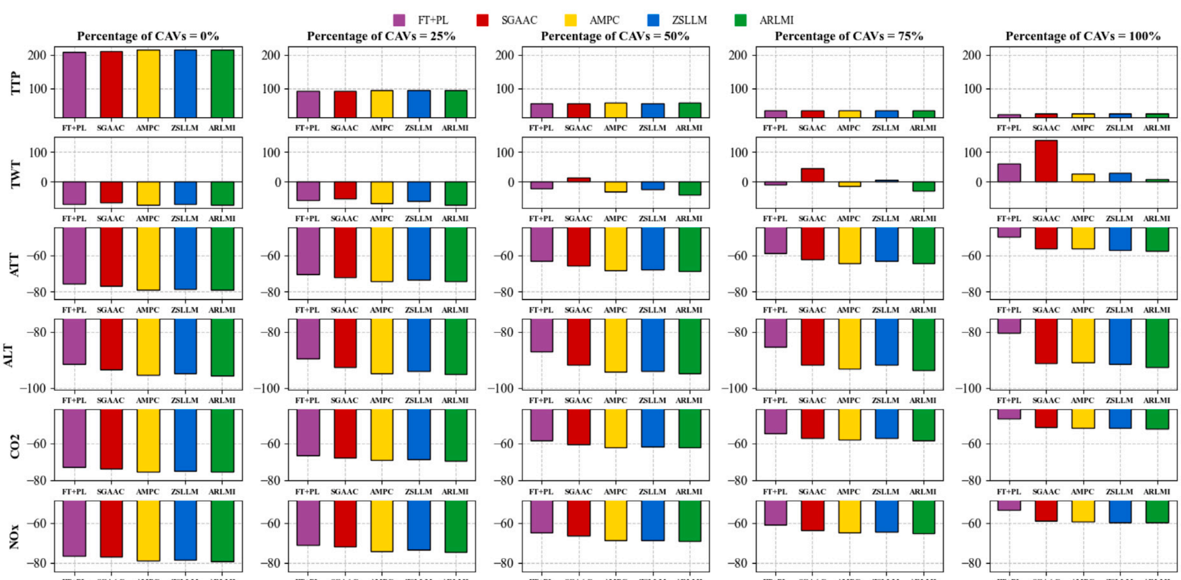

Fig. 10. Relative changes (%) of the different strategies compared to the **Fixed Time** scenario **Fixed-Time (FT), Fixed-Time + Platooning (FT+PL), SUMO Gap-Actuated Adaptive Control (SGAAC), Adaptive MPC (AMPC), Zero-Shot LLM Advisor (ZSLLM), Adaptive-Robust LMI-based control (ARLMI)** in presence of uncertainty.

across the chosen vertex set and recovering the feedback gain via the $\Gamma = KP$ change of variables, the method produces gains that are numerically amenable to semidefinite programming and that guarantee exponential decay of the queue-energy bound. In practice, this formal robustness translates into markedly smaller queue accumulations and improved throughput in the presence of parameter perturbations when compared to non-robust baselines. Importantly, this advantage remains evident when compared against stronger model-based adaptive baselines such as **AMPC**. While **AMPC** dynamically adjusts control inputs based on short-horizon predictions and online model estimation, it does not explicitly enforce robustness guarantees under structured uncertainty. As a result, although **AMPC** achieves competitive performance under nominal conditions, it may exhibit performance degradation when system parameters deviate from their estimated values. The SUMO-backed experiments using real arterial data show consistent performance gains for **ARLMI** across environmental metrics and travel-time measures, indicating that the Lyapunov certificate has useful operational consequences beyond asymptotic theory.

Second, the feedforward disturbance-rejection channel meaningfully reduces transient queue growth caused by near-term measurable inflow surges. By consuming short-horizon inflow and upstream indicators and distributing the expected inflow across the independent directions using a conservative allocation matrix L_{ff}, the controller can preemptively allocate green time to approaches that will receive sudden demand. This reduces the reactive burden on the feedback loop, lowers the magnitude of control corrections, and improves ride-through performance during demand spikes. The decomposition of per-direction increments, $\Delta u_j = \Delta u_{j,1} + \Delta u_{j,2}$, is practically convenient

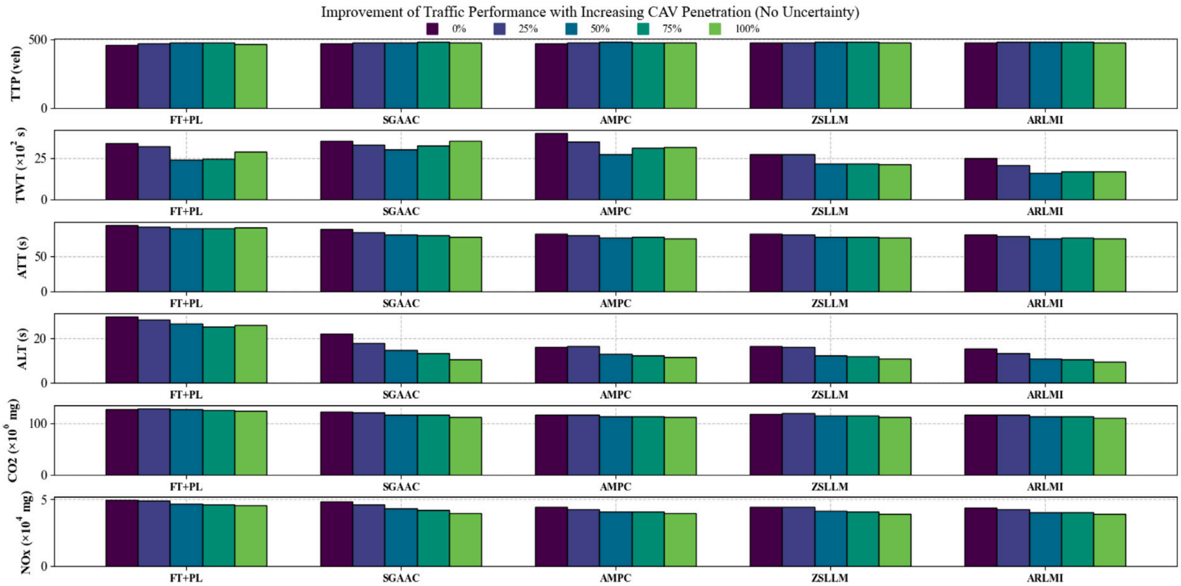

Fig. 11. Effect of CAV penetration rate on performance metrics under nominal conditions (without uncertainty).

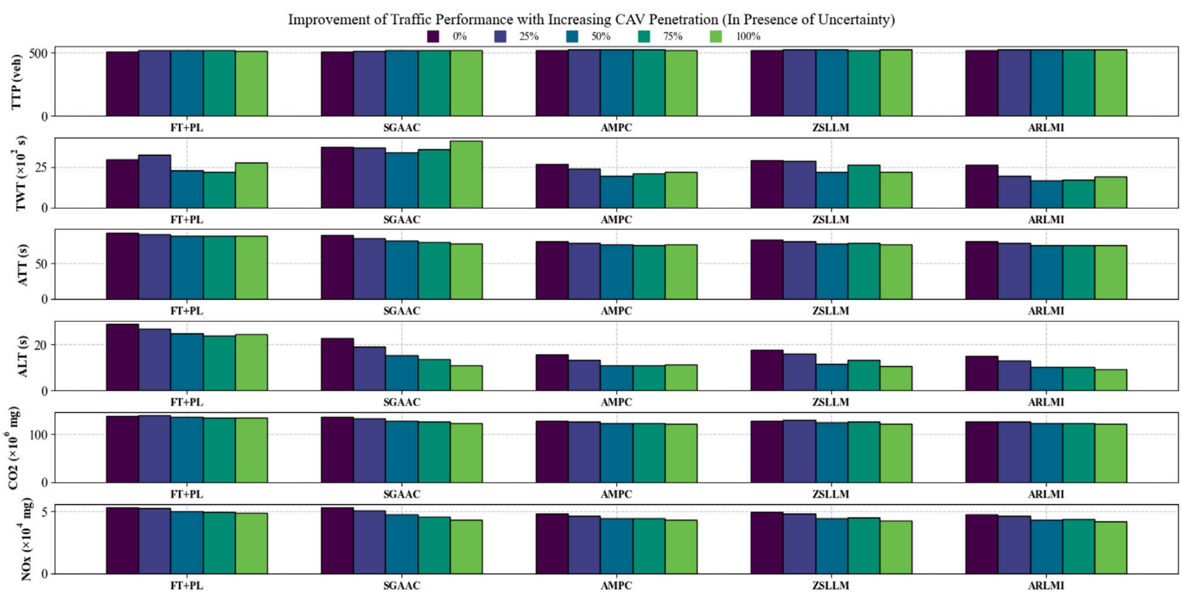

Fig. 12. Effect of CAV penetration rate on performance metrics in presence of uncertainty.

for implementation and clarifies the distinct roles of feedback (stability, long-run regulation) and feedforward (transient compensation).

Third, the adaptive operational layer, an identify-then-control scheme that estimates $B(n)$ from recent cycle data using a regularized least-squares estimator and triggers online LMI re-synthesis only when identification confidence and compute budget permit, achieves a favorable balance between adaptivity and computational feasibility. In our experiments, the adaptive loop successfully reduced conservatism when CAV penetration increased (thus reducing input mapping uncertainty), while retaining a safe fallback behavior through an LQR gain computed from a nominal B_{nom} whenever identification was unreliable or solver resources were constrained. This pragmatic design addresses a common practical concern with many adaptive robust schemes: the tension between rapid online adaptation and guaranteed safe performance when computation or data quality deteriorates. In contrast, **AMPC** follows a receding-horizon optimization strategy based on an implicitly updated system model, but without incorporating explicit robustness margins in the controller synthesis. This distinction highlights a key contribution of the proposed framework: the integration of online adaptation with formal robustness guarantees, which is not inherently present in standard adaptive MPC formulations.

Fourth, the computational profiling versus a zero-shot LLM advisor baseline highlights a critical implementation reality: AI-based advisors can offer promising ideas but often demand substantially higher inference and orchestration latency (and network dependency), which may compromise real-time actuation. In our platform-level tests, **ARLMI** required orders of magnitude less online processing time per cycle than the LLM-based scenario (**ZSLLM**).

However, it should be emphasized that the primary performance comparisons in this study are conducted against established traffic control strategies, including **SGAAC** and the model-based adaptive benchmark **AMPC**. The **ZSLLM** scenario is therefore included as a secondary reference to illustrate computational trade-offs rather than as a directly comparable control baseline. These findings support the

Table 3
Results without uncertainty. Absolute values of CO_2 (mg), NO_x (mg), ATT (s), ALT (s), TWT (s), and TTP (veh) across CAV penetration levels for each control scenario. (Each column corresponds to a CAV penetration level: 0%, 25%, 50%, 75%, 100%.)

Without Uncertainty						
Control Scenario	Parameter	Percentage of CAVs				
		0	25	50	75	100
Adaptive-Robust LMI-based Control	CO_2	116818399	116293451	113491458	113881993	111312345
	NO_x	43512.52	42342.3	40212.64	40266.93	38883.54
	ATT	81.44	78.91	76.13	76.34	75.84
	ALT	15.32	13.16	10.74	10.52	9.55
	TWT	2490	2045	1614	1672	1686
	TTP	474	480	483	482	477
Fixed Time	CO_2	475573667	387553063	297847541	261363788	241123955
	NO_x	210935.72	170511.87	128182.45	110823.49	100482.42
	ATT	390.16	305.13	241.74	203.47	184.77
	ALT	339.65	257.54	188.54	149.45	128.27
	TWT	5442	24279	3265	1929	2041
	TTP	155	237	310	370	391
Fixed Time + Platooning	CO_2	127921933	129069581	126667925	125585550	124862746
	NO_x	49265.95	48729.25	46749.28	45946.23	45336.74
	ATT	94.73	92.83	90.47	89.93	90.72
	ALT	29.62	28.29	26.49	25.35	25.76
	TWT	3381	3201	2406	2421	2843
	TTP	462	473	476	475	468
SUMO Gap-Actuated Adaptive Control	CO_2	123580130	120622245	117088954	116064689	112784209
	NO_x	48178.85	45798.39	43392.47	42171.28	39527.47
	ATT	89.3	84.98	81.61	80.17	77.73
	ALT	22.11	17.98	14.7	13.28	10.67
	TWT	3545	3273	2999	3240	3540
	TTP	469	478	478	482	475
Adaptive MPC	CO_2	116996476	117090558	113541064	113906473	111556728
	NO_x	44226.06	42720.3	40976.96	40957.75	39553.96
	ATT	82.49	79.65	76.77	78.29	75.76
	ALT	16.15	16.53	12.93	12.19	11.42
	TWT	3973	3477	2703	3081	3130
	TTP	470	475	480	479	478
Zero-Shot LLM Advisor	CO_2	118990341	119129566	115375922	114537056	111774112
	NO_x	44100.52	44184.46	41151.67	40621.75	39126.07
	ATT	81.85	81.63	77.96	77.75	77.08
	ALT	16.57	16.01	12.43	11.94	11.03
	TWT	2715	2712	2173	2178	2111
	TTP	474	476	483	482	476

Table 4
Relative results without uncertainty. Percentage change relative to the Fixed-Time baseline.

Without Uncertainty						
Control Scenario	Parameter	Percentage of CAVs				
		0	25	50	75	100
Adaptive-Robust LMI-based Control	CO_2	-75.44%	-70.00%	-61.89%	-56.43%	-53.84%
	NO_x	-79.37%	-75.17%	-68.63%	-63.67%	-61.30%
	ATT	-79.13%	-74.14%	-68.51%	-62.48%	-58.95%
	ALT	-95.49%	-94.89%	-94.30%	-92.96%	-92.55%
	TWT	-54.24%	-91.58%	-50.57%	-13.32%	-17.39%
	TTP	205.81%	102.53%	55.81%	30.27%	21.99%
Fixed Time + Platooning	CO_2	-73.10%	-66.70%	-57.47%	-51.95%	-48.22%
	NO_x	-76.64%	-71.42%	-63.53%	-58.54%	-54.88%
	ATT	-75.72%	-69.58%	-62.58%	-55.80%	-50.90%
	ALT	-91.28%	-89.02%	-85.95%	-83.04%	-79.91%
	TWT	-37.87%	-86.82%	-26.31%	25.51%	39.29%
	TTP	198.06%	99.58%	53.55%	28.38%	19.69%
SUMO Gap-Actuated Adaptive Control	CO_2	-74.01%	-68.88%	-60.69%	-55.59%	-53.23%
	NO_x	-77.16%	-73.14%	-66.15%	-61.95%	-60.66%
	ATT	-77.11%	-72.15%	-66.24%	-60.60%	-57.93%
	ALT	-93.49%	-93.02%	-92.20%	-91.11%	-91.68%
	TWT	-34.86%	-86.52%	-8.15%	67.96%	73.44%
	TTP	202.58%	101.69%	54.19%	30.27%	21.48%
Adaptive MPC	CO_2	-75.40%	-69.79%	-61.88%	-56.42%	-53.73%
	NO_x	-79.03%	-74.95%	-68.03%	-63.04%	-60.64%
	ATT	-78.86%	-73.90%	-68.24%	-61.52%	-59.00%
	ALT	-95.25%	-93.58%	-93.14%	-91.84%	-91.10%
	TWT	-26.99%	-85.68%	-17.21%	59.72%	53.36%
	TTP	203.23%	100.42%	54.84%	29.46%	22.25%
Zero-Shot LLM Advisor	CO_2	-74.98%	-69.26%	-61.26%	-56.18%	-53.64%
	NO_x	-79.09%	-74.09%	-67.90%	-63.35%	-61.06%
	ATT	-79.02%	-73.25%	-67.75%	-61.79%	-58.28%
	ALT	-95.12%	-93.78%	-93.41%	-92.01%	-91.40%
	TWT	-50.11%	-88.83%	-33.45%	12.91%	3.43%
	TTP	205.81%	100.84%	55.81%	30.27%	21.74%

view that lightweight control-theoretic designs with formal guarantees remain highly competitive for embedded, safety-critical urban control tasks.

Overall, the inclusion of **AMPC** as a representative adaptive model-based controller provides a more rigorous benchmark for evaluating the proposed approach. The results indicate that while both **AMPC** and **ARLMI** benefit from online adaptation, the explicit incorporation of robustness constraints in **ARLMI** leads to more consistent performance, particularly under uncertainty and demand fluctuations.

6. Conclusion and future works

This paper proposed a decentralized, two-level adaptive-robust control architecture for signalized intersections in mixed traffic environments. By combining macroscopic LMI-based robust synthesis with microscopic Connected and Autonomous Vehicles (CAVs) platooning, the framework effectively addresses the dual challenges of operational uncertainty and computational scalability. The core contributions include: (1) a Lyapunov-certified robust feedback design that guarantees stability under polytopic uncertainties; (2) a disturbance feedforward mechanism that exploits measurable inflows to improve transient response; and (3) an adaptive switching logic that leverages CAV penetration rates to dynamically optimize the trade-off between robustness and performance. Simulation results based on real-world traffic data confirmed that the proposed method significantly reduces delays and emissions compared to state-of-the-art benchmarks and offers a computationally superior alternative to LLM-based controllers for real-time applications.

For future work, several promising directions can be identified. A first and natural step is the field deployment of the proposed ARLMI controller and its validation through hardware-in-the-loop experiments on real traffic signal controllers or real-time PLC platforms, which would allow a systematic assessment of robustness against sensor degradation, communication jitter, and pedestrian-induced blocking under operational conditions. Beyond single or small arterial deployments, the two-level architecture can be generalized to larger urban networks, where its integration with Macroscopic Fundamental Diagram (MFD)-based perimeter control schemes could enable coordinated area-wide demand balancing while preserving the local LMI-based stability certificates. From a resilience perspective, future studies should also address adversarial and fault scenarios, including malicious sensor data and cyber-attacks on communication channels, by hardening the estimation and decision logic through anomaly detection and secure

Table 5
Results in presence of uncertainty. Absolute values for the same metrics and control scenarios when structured uncertainty is present in $B(n)$.

With Uncertainty						
Control Scenario	Parameter	Percentage of CAVs				
		0	25	50	75	100
Adaptive-Robust LMI-based Control	CO_2	127426230	126959231	123384018	123994124	121200143
	NO_x	47449.22	46219.95	43548.82	43833.77	42245.55
	ATT	80.82	79	75.75	76.25	75.39
	ALT	14.83	12.96	10.09	10.18	9.22
	TWT	2631	1926	1684	1729	1883
	TTP	518	524	526	525	523
Fixed Time	CO_2	515840103	413876763	328178104	296626536	252320402
	NO_x	229010.44	181209.16	141673.75	126370.88	105243.73
	ATT	387.51	309.62	240.93	214.16	176.89
	ALT	338.48	257.03	189.46	161.28	123.37
	TWT	12132	8419	2962	2465	1710
	TTP	164	268	335	390	415
Fixed Time + Platooning	CO_2	139125419	139195636	136510170	135158859	135022493
	NO_x	53388.76	52464.68	50163.45	49377.73	48882.18
	ATT	93.71	91.43	89.06	88.49	89.16
	ALT	28.79	26.67	24.81	23.68	24.34
	TWT	2940	3227	2292	2205	2780
	TTP	507	517	522	521	512
SUMO Gap-Actuated Adaptive Control	CO_2	136192405	133418276	129070481	127039109	123359544
	NO_x	53173.44	50782.25	47968.07	46100.76	43253.65
	ATT	89.6	86.16	82.27	80.57	77.45
	ALT	22.57	19.11	15.45	13.52	10.9
	TWT	3707	3692	3373	3595	4100
	TTP	510	516	521	520	520
Adaptive MPC	CO_2	127792963	127621070	123788559	124315933	121591211
	NO_x	48153.94	46703.74	44522.04	44696.66	43009.43
	ATT	81.8	79.62	76.96	76.25	77.26
	ALT	15.61	13.36	10.78	11.03	11.12
	TWT	2693	2402	1949	2112	2177
	TTP	518	524	525	524	522
Zero-Shot LLM Advisor	CO_2	129297409	129839181	124903874	126596356	121768731
	NO_x	49285.25	48217.98	44455	45234.25	42586.19
	ATT	83.13	81.61	77.48	78.92	76.43
	ALT	17.62	15.93	11.7	13.17	10.7
	TWT	2930	2859	2182	2642	2213
	TTP	517	524	524	522	523

Table 6
Relative results in the presence of uncertainty. Percentage change relative to the Fixed-Time baseline.

With Uncertainty						
Control Scenario	Parameter	Percentage of CAVs				
		0	25	50	75	100
Adaptive-Robust LMI-based Control	CO_2	-75.30%	-69.32%	-62.40%	-58.20%	-51.97%
	NO_x	-79.28%	-74.49%	-69.26%	-65.31%	-59.86%
	ATT	-79.14%	-74.48%	-68.56%	-64.40%	-57.38%
	ALT	-95.62%	-94.96%	-94.67%	-93.69%	-92.53%
	TWT	-78.31%	-77.12%	-43.15%	-29.86%	10.12%
	TTP	215.85%	95.52%	57.01%	34.62%	26.02%
Fixed Time + Platooning	CO_2	-73.03%	-66.37%	-58.40%	-54.43%	-46.49%
	NO_x	-76.69%	-71.05%	-64.60%	-60.93%	-53.56%
	ATT	-75.82%	-70.47%	-63.04%	-58.68%	-49.60%
	ALT	-91.49%	-89.62%	-86.90%	-85.32%	-80.27%
	TWT	-75.77%	-61.67%	-22.62%	-10.55%	62.57%
	TTP	209.15%	92.91%	55.82%	33.59%	23.37%
SUMO Gap-Actuated Adaptive Control	CO_2	-73.60%	-67.76%	-60.67%	-57.17%	-51.11%
	NO_x	-76.78%	-71.97%	-66.14%	-63.52%	-58.90%
	ATT	-76.88%	-72.17%	-65.85%	-62.38%	-56.22%
	ALT	-93.33%	-92.56%	-91.85%	-91.62%	-91.16%
	TWT	-69.44%	-56.15%	13.88%	45.84%	139.77%
	TTP	210.98%	92.54%	55.52%	33.33%	25.30%
Adaptive MPC	CO_2	-75.23%	-69.16%	-62.28%	-58.09%	-51.81%
	NO_x	-78.97%	-74.23%	-68.57%	-64.63%	-59.13%
	ATT	-78.89%	-74.28%	-68.06%	-64.40%	-56.32%
	ALT	-95.39%	-94.80%	-94.31%	-93.16%	-90.99%
	TWT	-77.80%	-71.47%	-34.20%	-14.32%	27.31%
	TTP	215.85%	95.52%	56.72%	34.36%	25.78%
Zero-Shot LLM Advisor	CO_2	-74.93%	-68.63%	-61.94%	-57.32%	-51.74%
	NO_x	-78.48%	-73.39%	-68.62%	-64.20%	-59.54%
	ATT	-78.55%	-73.64%	-67.84%	-63.15%	-56.79%
	ALT	-94.79%	-93.80%	-93.82%	-91.83%	-91.33%
	TWT	-75.85%	-66.04%	-26.33%	7.18%	29.42%
	TTP	215.24%	95.52%	56.42%	33.85%	26.02%

estimation techniques. Finally, the framework can be extended toward a human-in-the-loop, multi-objective tuning paradigm, in which emissions, delay, equity, and other policy-relevant criteria are explicitly traded off and traffic operators are provided with intuitive mechanisms to guide and adjust controller behavior for real-world adoption.

Another important direction for future research is the extension of the proposed framework to more complex intersection geometries and signal phase structures. In particular, real-world intersections often include protected turning phases, pedestrian crossings, and non-negligible clearance (lost) times between phases. These features can be incorporated into the proposed modeling and control framework by augmenting the system state and input vectors and redefining the phase structure accordingly. For example, protected turning movements can be modeled as additional control inputs with dedicated saturation flow parameters, while pedestrian phases can be represented as constrained intervals that impose additional timing requirements. Although such extensions increase the dimensionality of the system and the associated optimization problems, the underlying LMI-based synthesis and adaptive control structure remain applicable. Investigating scalable implementations and computational efficiency for these higher-dimensional settings constitutes an important direction for future work.

CRediT authorship contribution statement

Arshia Abdi: Writing – original draft, Software, Methodology, Data curation. **Bijan Moaveni:** Validation, Supervision, Methodology. **Tamás Tettamanti:** Writing – review & editing, Writing – original draft, Investigation, Conceptualization.

Declaration of AI-assisted technologies in the manuscript preparation process

During the preparation of this work the authors used Grammarly tool in order to check and improve the English grammar. After using this tool, the authors reviewed and edited the content as needed and take full responsibility for the content of the published article.

Declaration of competing interest

The authors declare that they have no known competing financial interests or personal relationships that could have appeared to influence the work reported in this paper.

Acknowledgments

The research was supported by the European Union within the framework of the National Laboratory for Autonomous Systems (RRF-2.3.1-21-2022-00002).

Appendix. Additional robustness and sensitivity analysis

In this appendix, we provide additional simulation results to complement the main experimental section and to further clarify the robustness and sensitivity properties of the proposed control framework. In particular, we explicitly separate the effects of (i) saturation flow uncertainty and (ii) inflow variations, and we report the system performance under multiple operating conditions.

Two distinct sources of uncertainty are considered in this work:

- **Exogenous inflow disturbances:** These correspond to variations in the arrival rates $q^{in}(n)$ and are treated as bounded disturbances in the closed-loop dynamics.
- **Parametric uncertainty in saturation flow rates:** This is modeled through the polytopic representation of the input matrix $B(n)$ as a convex combination of vertex matrices, as shown in Eq. (26). Each vertex matrix corresponds to an extreme realization of the saturation flow rates s_l under bounded uncertainty. Specifically, the vertices are defined as:
  - B_1: All approaches operate at upper-bound saturation flow rates, i.e., $s_l = (1+\delta)s_l^{\text{nom}}$:

$$B_1 = -\begin{bmatrix} (1+\delta)s_l^{\text{nom}} & 0 \\ 0 & (1+\delta)s_l^{\text{nom}} \\ (1+\delta)s_l^{\text{nom}} & 0 \\ 0 & (1+\delta)s_l^{\text{nom}} \end{bmatrix} \tag{A.1}$$

  - B_2: All approaches operate at lower-bound saturation flow rates, i.e., $s_l = (1-\delta)s_l^{\text{nom}}$:

$$B_2 = -\begin{bmatrix} (1-\delta)s_l^{\text{nom}} & 0 \\ 0 & (1-\delta)s_l^{\text{nom}} \\ (1-\delta)s_l^{\text{nom}} & 0 \\ 0 & (1-\delta)s_l^{\text{nom}} \end{bmatrix} \tag{A.2}$$

  - B_3: Horizontal approaches (1 and 3) operate at upper-bound saturation flow rates, while vertical approaches (2 and 4) operate at lower-bound rates:

$$B_3 = -\begin{bmatrix} (1+\delta)s_l^{\text{nom}} & 0 \\ 0 & (1-\delta)s_l^{\text{nom}} \\ (1+\delta)s_l^{\text{nom}} & 0 \\ 0 & (1-\delta)s_l^{\text{nom}} \end{bmatrix} \tag{A.3}$$

  - B_4: Horizontal approaches operate at lower-bound saturation flow rates, while vertical approaches operate at upper-bound rates:

$$B_4 = -\begin{bmatrix} (1-\delta)s_l^{\text{nom}} & 0 \\ 0 & (1+\delta)s_l^{\text{nom}} \\ (1-\delta)s_l^{\text{nom}} & 0 \\ 0 & (1+\delta)s_l^{\text{nom}} \end{bmatrix} \tag{A.4}$$

  In the simulations presented in this appendix, the uncertainty level is set to $\delta = 0.2$, corresponding to a $\pm 20\%$ variation around the nominal saturation flow rates. The resulting numerical values of the vertex matrices are:

$$B_1 = -\begin{bmatrix} 0.6 & 0 \\ 0 & 0.6 \\ 0.6 & 0 \\ 0 & 0.6 \end{bmatrix}, \quad B_2 = -\begin{bmatrix} 0.4 & 0 \\ 0 & 0.4 \\ 0.4 & 0 \\ 0 & 0.4 \end{bmatrix}, \tag{A.5a}$$

$$B_3 = -\begin{bmatrix} 0.6 & 0 \\ 0 & 0.4 \\ 0.6 & 0 \\ 0 & 0.4 \end{bmatrix}, \quad B_4 = -\begin{bmatrix} 0.4 & 0 \\ 0 & 0.6 \\ 0.4 & 0 \\ 0 & 0.6 \end{bmatrix}. \tag{A.5b}$$

  The vertex matrices $B_1, \ldots, B_4$ therefore represent extreme realizations of the saturation flow uncertainty set and are used to evaluate the robustness of the proposed controller under worst-case conditions.

The selection of the uncertainty bound $\delta = 0.2$ is motivated by both empirical observations and modeling considerations. The studied urban corridor in Tehran typically operates under high-demand conditions, where the network frequently approaches saturation during peak hours. In such regimes, variations in driver behavior, lane utilization, vehicle composition, and local disturbances can lead to noticeable fluctuations in effective saturation flow rates. Based on these observations, a $\pm 20\%$ variation around the nominal saturation flow is considered a realistic and practically relevant uncertainty range. This level of variation is sufficient to capture the impact of heterogeneous driving behavior and traffic disturbances without introducing excessively conservative assumptions. It is also important to note that adopting significantly larger uncertainty bounds (e.g., $\pm 50\%$) would imply highly unrealistic deviations from nominal traffic conditions and would lead to overly conservative controller designs. Therefore, the selected uncertainty set provides a balanced trade-off between realism and robustness, ensuring meaningful performance evaluation under representative operating conditions.

In the main text, these effects are analyzed separately: the LMI-based synthesis guarantees robustness with respect to parametric uncertainty in $B(n)$, while inflow variations are handled through feedforward compensation and disturbance rejection mechanisms. To evaluate the sensitivity of the proposed controller to saturation flow uncertainty, we conducted simulations for each vertex matrix B_i, $i = 1, \ldots, 4$, corresponding to different extreme realizations of the uncertainty set. For each scenario, the system performance is evaluated under varying initial green times and performance metrics introduced in Section 4 are recorded. The results are summarized in Fig. A.13 and Table A.7, where each block corresponds to a specific uncertainty realization.

To further improve the interpretability of the results presented in Fig. A.13 and Table A.7 provides a graphical representation of the same data. Each subplot illustrates the variation of a specific performance metric with respect to the initial green time under different uncertainty realizations. This visualization helps to better highlight performance trends and differences across scenarios, which may be less apparent in tabular form. In particular, it confirms that the proposed controller maintains consistent behavior across all uncertainty vertices, while preserving similar trends with respect to the initial signal timing.

These results demonstrate that our proposed method maintains stable and consistent performance across all uncertainty vertices. In particular, while variations in saturation flow rates affect absolute performance levels, the controller preserves stability and avoids performance degradation across all tested cases.

The results in Fig. A.13 and Table A.7 highlight several important observations:

- The proposed controller exhibits robust performance across all extreme uncertainty realizations, confirming the effectiveness of the polytopic LMI formulation.
- Performance trends remain consistent across different initial cycle times, indicating that the control strategy is not overly sensitive to the choice of signal timing parameters.
- The variation between best-case (B_1) and worst-case (B_2) scenarios is bounded, demonstrating that the controller effectively mitigates the impact of parameter uncertainty.
- Intermediate cases (B_3, B_4), which represent asymmetric uncertainty across directions, further confirm that the controller adapts well to heterogeneous traffic conditions.

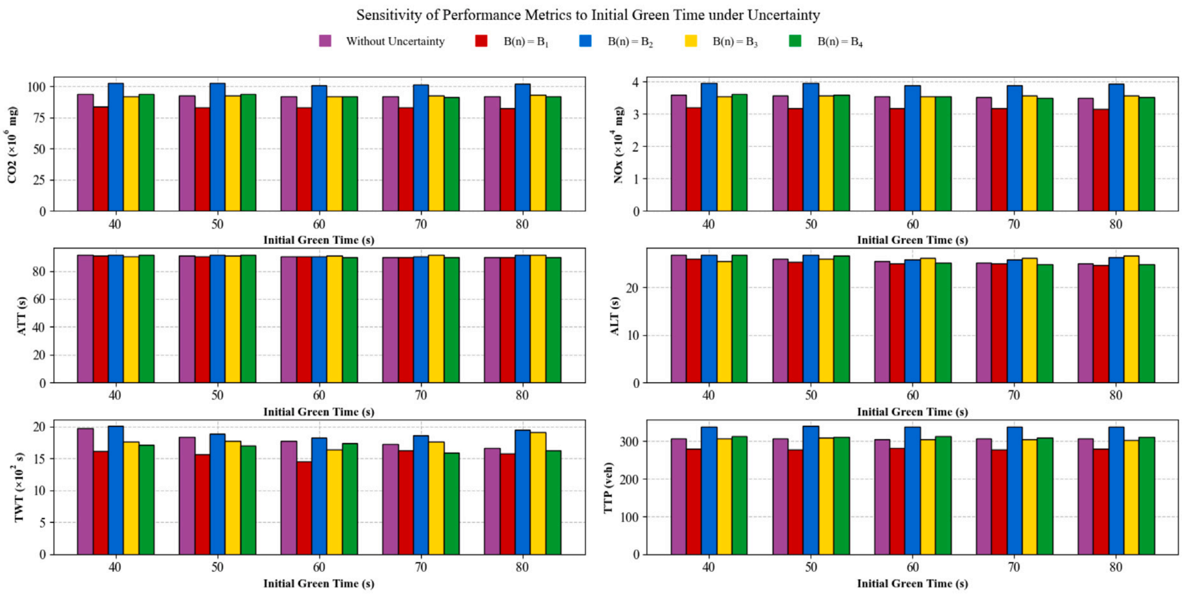

Fig. A.13. Sensitivity of key performance metrics (CO_2 (mg), NO_x (mg), ATT (s), ALT (s), TWT (s), and TTP (veh)) with respect to the initial green time under nominal conditions and different saturation flow uncertainty realizations ($B_1, \ldots, B_4$). Each subplot illustrates the variation of one metric as a function of the initial green time. The results complement Table A.7 by providing a visual comparison of performance trends across uncertainty scenarios, highlighting the robustness and consistency of the proposed controller.

Table A.7
Sensitivity analysis of the proposed controller under saturation flow uncertainty. Performance metrics (CO_2 (mg), NO_x (mg), ATT (s), ALT (s), TWT (s), and TTP (veh)) are reported for different initial green times under nominal conditions and for each uncertainty vertex $B_1, \ldots, B_4$ (corresponding to ±20% variation in saturation flow rates). This table isolates the effect of parametric uncertainty in $B(n)$ while keeping inflow conditions unchanged.

Initial Green Time			40	50	60	70	80
Without Uncertainty		CO_2	93618762	92875515	92180362	92082148	91665801
		NO_x	36037.1	35670.57	35348.41	35323.59	35061.39
		ATT	91.49	90.86	90.4	90.1	89.69
		ALT	26.87	25.98	25.56	25.23	24.92
		TWT	1973	1836	1769	1719	1663
		TTP	308	308	306	308	307
In presence of Uncertainty	B(n) = B 1	CO_2	83676479	83298539	82897505	82993666	82795284
		NO_x	32115.8	31904.91	31736.38	31759.62	31653.08
		ATT	91.05	90.54	90.2	90.09	89.83
		ALT	25.93	25.38	25.06	24.96	24.61
		TWT	1609	1566	1455	1622	1576
		TTP	280	278	282	278	280
	B(n) = B 2	CO_2	102626916	102846059	101109109	101449766	102119452
		NO_x	39578.36	39635.84	38854.72	38976.38	39240.58
		ATT	91.82	91.64	90.72	90.56	91.38
		ALT	26.84	26.84	25.8	25.73	26.36
		TWT	2002	1881	1816	1853	1949
		TTP	339	340	338	338	338
	B(n) = B 3	CO_2	92153421	92670470	92109144	92766354	93095107
		NO_x	35417.97	35598.84	35393.45	35608.38	35765.9
		ATT	90.66	91.08	91.23	91.4	91.78
		ALT	25.43	25.99	26.17	26.2	26.64
		TWT	1760	1772	1639	1764	1902
		TTP	308	309	305	306	304
	B(n) = B 4	CO_2	94007066	93684513	92225943	91550303	92004529
		NO_x	36209.26	36038.16	35358.13	35032.47	35220.02
		ATT	91.74	91.59	89.99	89.64	89.8
		ALT	26.82	26.65	25.13	24.76	24.83
		TWT	1707	1701	1737	1586	1624
		TTP	313	311	313	310	312

It is important to note that the results presented in this appendix primarily reflect the effect of the feedback component under varying uncertainty realizations. In particular, since the uncertainty is introduced through $B(n)$, the robustness properties demonstrated here are directly attributable to the LMI-based feedback design. The feedforward component, on the other hand, is designed to mitigate inflow disturbances and primarily affects transient performance rather than robustness to parametric uncertainty. Therefore, the results in this appendix implicitly illustrate the contribution of the feedback controller in handling structural uncertainty in the system dynamics.

Overall, the additional results presented in this appendix confirm that the proposed control framework achieves robust and consistent performance under a wide range of uncertainty realizations and operating conditions. These findings complement the main simulation results and further support the effectiveness of the proposed adaptive robust control architecture.

References

[1] S.V. Ukkusuri, G. Ramadurai, G. Patil, A robust transportation signal control problem accounting for traffic dynamics, Comput. Oper. Res. 37 (5) (2010) 869–879.
[2] G. Zhang, Y. Wang, Optimizing minimum and maximum green time settings for traffic actuated control at isolated intersections, IEEE Trans. Intell. Transp. Syst. 12 (1) (2010) 164–173.
[3] A. Sysoev, S. Zhikhoreva, V. Klyavin, A. Pogodaev, Neural networks approach to remodel capacity on urban road and street network, Period. Polytech. Transp. Eng. 53 (4) (2025) 357–363, http://dx.doi.org/10.3311/PPtr.37194.
[4] J. Chodur, K. Ostrowski, M. Tracz, Impact of saturation flow changes on performance of traffic lanes at signalised intersections, Procedia-Social Behav. Sci. 16 (2011) 600–611.
[5] T. Tettamanti, I. Varga, T. Péni, T. Luspay, B. Kulcsár, Uncertainty modeling and robust control in urban traffic, IFAC Proc. Vol. 44 (1) (2011) 14910–14915.
[6] T. Tettamanti, T. Luspay, B. Kulcsar, T. Péni, I. Varga, Robust control for urban road traffic networks, IEEE Trans. Intell. Transp. Syst. 15 (1) (2013) 385–398.
[7] W. Xiang, J. Xiao, Y. Jiang, Real-time signalization for an oversaturated intersection via static state feedback control: A switched system approach, J. Franklin Inst. 352 (8) (2015) 3304–3324.
[8] V.S.S. Rajampalli, A.R. Narra, et al., A spatio-temporal GNN and multi-agent system framework for bottleneck prediction and signal optimization in Bangalore, Results Eng. (2025) 107675.
[9] F. Harrou, A. Zeroual, F. Kadri, Y. Sun, Enhancing road traffic flow prediction with improved deep learning using wavelet transforms, Results Eng. 23 (2024) 102342.

[10] J. Haddad, B. Mirkin, Adaptive perimeter traffic control of urban road networks based on MFD model with time delays, Internat. J. Robust Nonlinear Control 26 (6) (2016) 1267–1285.
[11] J. Haddad, B. Mirkin, Coordinated distributed adaptive perimeter control for large-scale urban road networks, Transp. Res. Part C: Emerg. Technol. 77 (2017) 495–515.
[12] M. Malekzadeh, M. Naderi, F. Jin, K. Bogenberger, Y. Wang, M. Papageorgiou, A comprehensive review of tidal traffic flow control: From conventional lane reversal to emerging internal boundary control, Results Eng. (2025) 106198.
[13] S. Lin, B. De Schutter, Controller design for stabilizing bilinear systems with state-based switching, Nonlinear Anal. Hybrid Syst. 41 (2021) 101009.
[14] S. Huang, D. Sun, X. Liu, M. Zhao, H. Zhao, X. Liao, Observer-based double closed-loop control for mixed vehicle groups: a macro and micro perspective, IEEE Trans. Intell. Transp. Syst. 23 (10) (2022) 18129–18144.
[15] F. Khosrosereshki, B. Moaveni, Model validation and robust state feedback control for nonlinear subway traffic networks, ISA Trans. 148 (2024) 12–23.
[16] Z. Zhou, B. De Schutter, S. Lin, Y. Xi, Two-level hierarchical model-based predictive control for large-scale urban traffic networks, IEEE Trans. Control Syst. Technol. 25 (2) (2016) 496–508.
[17] T. Tettamanti, A. Mohammadi, H. Asadi, I. Varga, A two-level urban traffic control for autonomous vehicles to improve network-wide performance, Transp. Res. Procedia 27 (2017) 913–920.
[18] A. Kouvelas, D. Triantafyllos, N. Geroliminis, Two-layer hierarchical control for large-scale urban traffic networks, in: 2018 European Control Conference, ECC, IEEE, 2018, pp. 1295–1300.
[19] A. Rammohan, et al., Edge-driven resource allocation in vehicular networks: A joint framework of multi-agent reinforcement learning and demand-supply predictive modeling, Results Eng. (2025) 106100.
[20] G.S. van de Weg, M. Keyvan-Ekbatani, A. Hegyi, S.P. Hoogendoorn, Linear MPC-based urban traffic control using the link transmission model, IEEE Trans. Intell. Transp. Syst. 21 (10) (2019) 4133–4148.
[21] K. Stoilova, T. Stoilov, Model predictive traffic control by bi-level optimization, Appl. Sci. 12 (9) (2022) 4147.
[22] S. Wu, Z. Chen, S. Shen, J. Shen, F. Guo, Y. Liu, Y. Zhang, Hierarchical cooperative eco-driving control for connected autonomous vehicle platoon at signalized intersections, IET Intell. Transp. Syst. 17 (8) (2023) 1560–1574.
[23] W. Zhao, M. Yildirimoglu, A scalable macro–micro approach for cooperative platoon merging in mixed traffic flows, Transp. Res. Part C: Emerg. Technol. 169 (2024) 104859.
[24] C.B. Rafter, B. Anvari, S. Box, T. Cherrett, Augmenting traffic signal control systems for urban road networks with connected vehicles, IEEE Trans. Intell. Transp. Syst. 21 (4) (2020) 1728–1740.
[25] A. Sherly, M.S. Christo, J.V. Elizabeth, A hybrid approach to time series forecasting: Integrating ARIMA and prophet for improved accuracy, Results Eng. (2025) 105703.
[26] E. Papapanagiotou, F. Busch, Extended observer for urban traffic control based on limited measurements from connected vehicles, IEEE Trans. Intell. Transp. Syst. 21 (4) (2019) 1664–1676.
[27] Z. Sun, J. Dai, A. Ji, Z. Qin, W. Bu, Joint optimization of signal control and speed planning at isolated mixed-traffic signalized intersections, Appl. Soft Comput. (2025) 113493.
[28] Y. Shi, H. Dong, C.R. He, Y. Chen, Z. Song, Mixed vehicle platoon forming: A multiagent reinforcement learning approach, IEEE Internet Things J. 12 (11) (2025) 16886–16898.
[29] S.S. Mousavi, S. Bahrami, A. Kouvelas, Synthesis of output-feedback controllers for mixed traffic systems in presence of disturbances and uncertainties, IEEE Trans. Intell. Transp. Syst. 24 (6) (2022) 6450–6462.
[30] S.S. Mousavi, S. Bahrami, A. Kouvelas, Controller design for a mixed traffic system travelling at different desired speeds, Eur. J. Control 68 (2022) 100698.
[31] S.S. Mousavi, S. Bahrami, A. Kouvelas, A gain-scheduled robust H∞ control for a mixed traffic system travelling at different desired speeds in the presence of delay, in: 2022 IEEE 61st Conference on Decision and Control, CDC, IEEE, 2022, pp. 1156–1161.
[32] Y. Zheng, S.E. Li, K. Li, W. Ren, Platooning of connected vehicles with undirected topologies: Robustness analysis and distributed H-infinity controller synthesis, IEEE Trans. Intell. Transp. Syst. 19 (5) (2017) 1353–1364.
[33] Y. Li, C. Tang, S. Peeta, Y. Wang, Nonlinear consensus-based connected vehicle platoon control incorporating car-following interactions and heterogeneous time delays, IEEE Trans. Intell. Transp. Syst. 20 (6) (2018) 2209–2219.
[34] J. Nan, Z. Ge, X. Ye, A.F. Burke, J. Zhao, Model predictive control for autonomous vehicle path tracking through optimized kinematics, Results Eng. 24 (2024) 103123.
[35] M.H. Rahman, M.M. Gulzar, T.S. Haque, S. Habib, A. Shakoor, A.F. Murtaza, Trajectory planning and tracking control in autonomous driving system: Leveraging machine learning and advanced control algorithms, Eng. Sci. Technol. Int. J. 64 (2025) 101950.
[36] J. Wang, X. Luo, J. Yan, X. Guan, Distributed integrated sliding mode control for vehicle platoons based on disturbance observer and multi power reaching law, IEEE Trans. Intell. Transp. Syst. 23 (4) (2020) 3366–3376.
[37] J. Liang, L. Liu, X. Yu, W. Wang, C. Pan, L. Chen, Cooperative control of mixed CAV-HDV platoons with hierarchical optimization for oscillation mitigation, Phys. A (2025) 130844.
[38] P. Zhao, Y.D. Wong, F. Zhu, Modeling the clustering strength of connected autonomous vehicles and its impact on mixed traffic capacity, Commun. Transp. Res. 4 (2024) 100151.
[39] I.O. Olayode, A. Severino, F.J. Alex, E. Jamei, Traffic flow modelling of vehicles on a six lane freeway: Comparative analysis of improved group method of data handling and artificial neural network model, Results Eng. 25 (2025) 104094.
[40] J. Peng, W. Shangguan, L. Chai, J. Chen, C. Peng, B. Cai, V2X-enabled platoon control for aperiodic congestion mitigation via moving bottlenecks in mixed traffic environments, IEEE Trans. Veh. Technol. (2025).
[41] J. Peng, W. Shangguan, J. Chen, C. Peng, M.A. Arman, B. Cai, C.M. Tampére, Two-stage adaptive CAV control for mitigating congestion in mixed traffic environments using front-tracking method, Expert. Syst. Appl. 296 (2026) 129013.
[42] M. Malekzadeh, V.K. Yanumula, I. Papamichail, M. Papageorgiou, Overlapping internal boundary control of lane-free automated vehicle traffic, Control Eng. Pract. 133 (2023) 105435.
[43] S. Mobayen, M.T. Vu, R. Rahmani, H. Toshani, W. Assawinchaichote, P. Skruch, Constrained optimal formation control for nonlinear multi-agent systems using data-driven adaptive neural networks, Eng. Sci. Technol. Int. J. 73 (2026) 102269.
[44] H. Wang, M. Zhu, W. Hong, C. Wang, G. Tao, Y. Wang, Optimizing signal timing control for large urban traffic networks using an adaptive linear quadratic regulator control strategy, IEEE Trans. Intell. Transp. Syst. 23 (1) (2020) 333–343.
[45] N. Gupta, G.R. Patil, H.L. Vu, Efficacy of decentralized traffic signal controllers on stabilizing heterogeneous urban grid network, Commun. Transp. Res. 4 (2024) 100137.
[46] Y. Wang, D. Wang, S. Jin, N. Xiao, Y. Li, E. Frazzoli, Iterative tuning with reactive compensation for urban traffic signal control, IEEE Trans. Control Syst. Technol. 25 (6) (2016) 2047–2059.
[47] J. Zhou, D. Tian, Z. Sheng, X. Duan, G. Qu, D. Zhao, D. Cao, X. Shen, Robust min-max model predictive vehicle platooning with causal disturbance feedback, IEEE Trans. Intell. Transp. Syst. 23 (9) (2022) 15878–15897.
[48] P.A. Lopez, M. Behrisch, L. Bieker-Walz, J. Erdmann, Y.-P. Flötteröd, R. Hilbrich, L. Lücken, J. Rummel, P. Wagner, E. Wießner, Microscopic traffic simulation using SUMO, in: 2018 21st International Conference on Intelligent Transportation Systems, ITSC, Ieee, 2018, pp. 2575–2582.
[49] S. Xiao, X. Ge, Q.-L. Han, Y. Zhang, Dynamic event-triggered platooning control of automated vehicles under random communication topologies and various spacing policies, IEEE Trans. Cybern. 52 (11) (2021) 11477–11490.
[50] M. Rahimzadeh, H. Javanmardi, A. Hamedi, Constraint nonlinear model predictive control for trajectory tracking of a quadrotor using linear matrix inequalities, Results Eng. (2025) 107963.
[51] C.-q. Shao, J. Rong, X.-m. Liu, Study on the saturation flow rate and its influence factors at signalized intersections in China, Procedia-Social Behav. Sci. 16 (2011) 504–514.
[52] M.M. Coşkun, C. Şener, İ.H. Toroslu, Traffic signal optimization using multiobjective linear programming for oversaturated traffic conditions, Turk. J. Electr. Eng. Comput. Sci. 32 (1) (2024) 1–20.
[53] H.K. Khalil, Lyapunov stability, Control Syst. Robotics Autom. 12 (2009) 115.
[54] M. Neely, Stochastic Network Optimization with Application to Communication and Queueing Systems, Morgan & Claypool Publishers, 2010.
[55] X. Wang, Y. Yin, Y. Feng, H.X. Liu, Learning the max pressure control for urban traffic networks considering the phase switching loss, Transp. Res. Part C: Emerg. Technol. 140 (2022) 103670.
[56] F. Zhang, The Schur Complement and Its Applications, vol. 4, Springer Science & Business Media, 2006.
[57] D. Calvetti, S. Morigi, L. Reichel, F. Sgallari, Tikhonov regularization and the L-curve for large discrete ill-posed problems, J. Comput. Appl. Math. 123 (1–2) (2000) 423–446.

Arshia Abdi received the B.Sc. and M.Sc. degrees in control engineering from K. N. Toosi University of Technology, Tehran, Iran, in 2019 and 2021, respectively. He is currently pursuing a Ph.D. degree. His research interests include urban traffic control, large-scale systems, multi-input multi-output control systems, and system identification. During his studies, he has contributed to several research projects and scientific papers in the fields of road traffic modeling and intelligent transportation systems.

Bijan Moaveni received a B.Sc. degree in control engineering from the Isfahan University of Technology, Isfahan, Iran, in 2000, and the M.Sc. and Ph.D. degrees in control engineering from the K. N. Toosi University of Technology, Tehran, Iran, in 2002 and 2007, respectively. From 2009 to 2018, he served as an Assistant and Associate Professor in the Control and Signaling Department at the School of Railway Engineering, Iran University of Science and Technology, Tehran, Iran. He is now an Associate Professor with the System and Control group, Faculty of Electrical Engineering, K. N. Toosi University of Technology, Tehran, Iran. He is a member of the Center of Excellence for Modelling and Control of Complex Systems. Additionally, he serves as the head of the Complex Systems research laboratory. He has authored two books with Springer and John Wiley, as well as over 120 research articles.

Tamás Tettamanti received the Ph.D. (Budapest University of Technology and Economics) and D.Sc. (Hungarian Academy of Sciences) degrees in traffic engineering in 2013 and 2023, respectively. He acts as a full professor at the Budapest University of Technology and Economics, Faculty of Transportation Engineering and Vehicle Engineering. He participates in research and industrial projects both as a researcher and project coordinator. He is the co-author of over 180 scientific papers, two patents, and several books. His primary research interests include road traffic modeling, estimation, and control in the field of Cooperative, Connected, and Automated Mobility (CCAM), as well as related developments in co-simulation technology. He is a member of the Public Body of the Hungarian Academy of Sciences. He serves as an Editorial Board Member with IEEE Transactions on Intelligent Transportation Systems and Communications in Transportation Research journal. He is a member of the Technical Committee "TC 7.4 Transportation Systems" at IFAC (International Federation of Automatic Control).